



AFRL-RY-WP-TR-2019-0258

**ASSESSMENT OF RESIDUAL NONUNIFORMITY ON
HYPERSPSCTRAL TARGET DETECTION
PERFORMANCE**

**Joseph Meola
EO Target Detection & Surveillance Branch
Multispectral Sensing & Detection Division**

**Carl Joseph Cusumano
University of Dayton Research Institute**

**NOVEMBER 2019
Final Report**

Approved for public release; distribution is unlimited.

See additional restrictions described on inside pages

© 2019 University of Dayton Research Institute

STINFO COPY

**AIR FORCE RESEARCH LABORATORY
SENSORS DIRECTORATE
WRIGHT-PATTERSON AIR FORCE BASE, OH 45433-7320
AIR FORCE MATERIEL COMMAND
UNITED STATES AIR FORCE**

REPORT DOCUMENTATION PAGE				<i>Form Approved</i> OMB No. 0704-0188	
<p>The public reporting burden for this collection of information is estimated to average 1 hour per response, including the time for reviewing instructions, searching existing data sources, gathering and maintaining the data needed, and completing and reviewing the collection of information. Send comments regarding this burden estimate or any other aspect of this collection of information, including suggestions for reducing this burden, to Department of Defense, Washington Headquarters Services, Directorate for Information Operations and Reports (0704-0188), 1215 Jefferson Davis Highway, Suite 1204, Arlington, VA 22202-4302. Respondents should be aware that notwithstanding any other provision of law, no person shall be subject to any penalty for failing to comply with a collection of information if it does not display a currently valid OMB control number. PLEASE DO NOT RETURN YOUR FORM TO THE ABOVE ADDRESS.</p>					
1. REPORT DATE (DD-MM-YY) November 2019		2. REPORT TYPE Thesis		3. DATES COVERED (From - To) 24 September 2019 –24 September 2019	
4. TITLE AND SUBTITLE ASSESSMENT OF RESIDUAL NONUNIFORMITY ON HYPERSPETRAL TARGET DETECTION PERFORMANCE				5a. CONTRACT NUMBER FA8650-17-D-1801	
				5b. GRANT NUMBER	
				5c. PROGRAM ELEMENT NUMBER 63203F	
6. AUTHOR(S) Joseph Meola (AFRL/RMYT) Carl Joseph Cusumano (University of Dayton Research Institute)				5d. PROJECT NUMBER 665A	
				5e. TASK NUMBER N/A	
				5f. WORK UNIT NUMBER Y1H6	
7. PERFORMING ORGANIZATION NAME(S) AND ADDRESS(ES) Air Force Research Laboratory Sensors Directorate (AFRL/RMYT) Wright-Patterson Air Force Base, OH 45433-7320 Air Force Materiel Command United States Air Force				8. PERFORMING ORGANIZATION REPORT NUMBER University of Dayton Research	
9. SPONSORING/MONITORING AGENCY NAME(S) AND ADDRESS(ES) Air Force Research Laboratory Sensors Directorate Wright-Patterson Air Force Base, OH 45433-7320 Air Force Materiel Command United States Air Force				10. SPONSORING/MONITORING AGENCY ACRONYM(S) AFRL/RMYT	
				11. SPONSORING/MONITORING AGENCY REPORT NUMBER(S) AFRL-RY-WP-TR-2019-0258	
12. DISTRIBUTION/AVAILABILITY STATEMENT Approved for public release; distribution is unlimited.					
13. SUPPLEMENTARY NOTES PAO case number 88ABW-2019-4590, Clearance Date 24 September 2019. © 2019 University of Dayton Research Institute. Submitted in partial fulfillment of the requirements for the degree of Master of Science in Electrical Engineering at the University of Dayton School of Engineering. The U.S. Government is joint author of this work and has the right to use, modify, reproduce, release, perform, display, or disclose the work. Report contains color.					
14. ABSTRACT <p>Hyperspectral imaging sensors suffer from pixel-to-pixel response non-uniformity that manifests as fixed pattern noise (FPN) in collected data. FPN is typically removed by application of flat-field calibration procedures and non-uniformity correction algorithms. Despite application of these techniques, some amount of residual fixed pattern noise (RFPN) may persist in the data, negatively impacting target detection performance. In this work we examine the conditions under which RFPN can impact detection performance using data collected in the SWIR across a range of target materials. We designed and conducted a unique tower-based experiment where we carefully selected target materials that have varying degrees of separability from natural grass backgrounds. Furthermore, we designed specially-shaped targets for this experiment that introduce controlled levels of mixing between the target and background materials to support generation of high fidelity receiver operating characteristic (ROC) curves in our detection analysis. We perform several studies using this collected data. First, we assess the detection performance after a conventional non-uniformity correction. We then apply several scene-based non-uniformity correction (SB-NUC) algorithms from the literature and assess their abilities to improve target detection performance as a function of material separability. Then, we introduced controlled RFPN and study its adverse effects on target detection performance as well as the SBNUC techniques' ability to remove it. We demonstrate how residual fixed pattern noise affects the detectability of each target class differently based upon its inherent separability from the background. A moderate inherently separable material from the background is affected the most by the inclusion of SBNUC algorithms.</p>					
15. SUBJECT TERMS hyperspectral, non-uniformity correction					
16. SECURITY CLASSIFICATION OF:			17. LIMITATION OF ABSTRACT: SAR	18. NUMBER OF PAGES 62	19a. NAME OF RESPONSIBLE PERSON (Monitor) Joseph Meola 19b. TELEPHONE NUMBER (Include Area Code) N/A
a. REPORT Unclassified	b. ABSTRACT Unclassified	c. THIS PAGE Unclassified			

ASSESSMENT OF RESIDUAL NONUNIFORMITY ON HYPERSPECTRAL TARGET
DETECTION PERFORMANCE

Thesis
Submitted to
The School of Engineering of the
UNIVERSITY OF DAYTON

In Partial Fulfillment of the Requirements for
The Degree of
Master of Science in Electrical Engineering

By
Carl Joseph Cusumano

UNIVERSITY OF DAYTON

Dayton, Ohio

August, 2019

ASSESSMENT OF RESIDUAL NONUNIFORMITY ON HYPERSPECTRAL TARGET
DETECTION PERFORMANCE

Name: Cusumano, Carl Joseph

APPROVED BY:

Bradley M. Ratliff, Ph.D.
Advisory Committee Chairman
Associate Professor and Chair,
Electrical and Computer Engineering

Jason R. Kaufman, Ph.D.
Committee Member
Adjunct Professor, Electrical and
Computer Engineering

Eric J. Balster, Ph.D.
Committee Member
Dean of Electrical and Computer
Engineering, Electrical and
Computer Engineering

Robert J. Wilkens, Ph.D., P.E.
Associate Dean for Research and Innovation
Professor
School of Engineering

Eddy M. Rojas, Ph.D., M.A., P.E.
Dean, School of Engineering

© Copyright by
Carl Joseph Cusumano
All rights reserved
2019

ABSTRACT

ASSESSMENT OF RESIDUAL NONUNIFORMITY ON HYPERSPECTRAL TARGET DETECTION PERFORMANCE

Name: Cusumano, Carl Joseph
University of Dayton

Advisor: Dr. Bradley M. Ratliff

Hyperspectral imaging sensors suffer from pixel-to-pixel response nonuniformity that manifests as fixed pattern noise (FPN) in collected data. FPN is typically removed by application of flat-field calibration procedures and nonuniformity correction algorithms. Despite application of these techniques, some amount of residual fixed pattern noise (RFPN) may persist in the data, negatively impacting target detection performance. In this work we examine the conditions under which RFPN can impact detection performance using data collected in the SWIR across a range of target materials. We designed and conducted a unique tower-based experiment where we carefully selected target materials that have varying degrees of separability from natural grass backgrounds. Furthermore, we designed specially-shaped targets for this experiment that introduce controlled levels of mixing between the target and background materials to support generation of high fidelity receiver operating characteristic (ROC) curves in our detection analysis. We perform several studies using this collected data. First, we assess the detection performance after a conventional nonuniformity correction. We then apply several scene-based nonuniformity correction (SBNUC) algorithms from the literature and assess their abilities to improve target detection performance as a function of material separability. Then, we introduced controlled RFPN and study its adverse affects on target detection performance as well as the SBNUC techniques' ability to remove it. We demonstrate how residual fixed pattern noise affects the

detectability of each target class differently based upon its inherent separability from the background. A moderate inherently separable material from the background is affected the most by the inclusion of SBNUC algorithms.

Dedicated to my family for their endless support and encouragement throughout my
academic career.

ACKNOWLEDGMENTS

I would like to give a special thanks to my advisor, Dr. Bradley Ratliff. Dr. Ratliff is an excellent researcher and has proved so time and time again during his time mentoring me. His insights have helped me grow on an academic, professional, and also personal level that I will never forget.

I would also like to thank Dr. Jason Kaufman for mentoring me throughout my research work. His expertise and willingness to provide me with support has allowed me to be successful inside and outside the classroom.

I would like to thank Dr. Eric Balster for being a committee member and an outstanding resource throughout my time here at the University of Dayton.

I would like to thank Dr. Joe Meola and the AFRL team for funding this project under contract number FA8650-17-D-1801 and providing me with the opportunity to grow in my academics.

Lastly I would like to thank Ratliff Metal Spinning Co., Inc. for their donation of time and materials in the creation of the mixture targets for this work.

TABLE OF CONTENTS

ABSTRACT	iii
DEDICATION	v
ACKNOWLEDGMENTS	vi
LIST OF FIGURES	viii
LIST OF TABLES	x
CHAPTER I. INTRODUCTION	1
CHAPTER II. SENSOR MODELING & SBNUC APPROACH	5
2.1 Sensor Model	5
2.2 Algorithm Descriptions	7
CHAPTER III. DATA COLLECTION PLANNING	11
3.1 Material Selection	13
3.2 Target Mixture Simulation & Fabrication	15
3.3 Collection Scenario and Conditions	19
CHAPTER IV. DATA PROCESSING & EXPLOITATION	24
CHAPTER V. DETECTION PERFORMANCE	28
5.1 Detection Performance on Collected Data	29
5.2 Target Detection Performance as a Function of RFPN	33
CHAPTER VI. CONCLUSION	46
BIBLIOGRAPHY	48

LIST OF FIGURES

2.1	Hyperspectral Sensor Model with its Corresponding Image Cube	5
2.2	NRL Algorithm	10
3.1	Theoretical Target vs Background Histogram Distribution	12
3.2	Materials Selected for the Data Collection	15
3.3	Mixture Simulation Graphical Representation	17
3.4	Simulated Imagery from the Target Mixture Simulation	18
3.5	Target Array Layout	20
3.6	Imagery of Each Scenario from the Data Collection	21
3.7	Imagery of the Sensor, Tower, and Target Array	22
3.8	Single Band Image from Each Scenario	23
4.1	L1 Corrected Cubes and Their Corresponding RX Maps	26
4.2	Truth and Grass Masks	27
5.1	ROC Curves Categorized by Target Material	30
5.2	ROC Curves Categorized by SBNUC Algorithm	31
5.3	ACE Histograms Generated after SBNUC Algorithms Applied	33
5.4	Band Images with Corresponding RX Maps of Varying Noise Levels Introduced	35
5.5	ROC Curves Generated after Noise Introduction	36
5.6	ACE Histograms of Varying Noise Levels Introduced of the Sawdust and Sand Classes	39
5.7	ACE Histograms of Varying Noise Levels Introduced of the Tan Latex and Red Plasti-Dip [®] Classes	40
5.8	Band Images with Corresponding RX Maps of Varying Noise Levels SBNUC Corrected	41

5.9	ROC Curves Generated after Noise Introduction and SBNUC Correction . . .	42
5.10	ACE Histograms of Varying Noise Levels SBNUC Corrected of the Sawdust and Sand Classes	43
5.11	ACE Histograms of Varying Noise Levels SBNUC Corrected of the Tan Latex and Red Plasti-Dip [®] Classes	44
5.12	Theoretical Target/Background ACE Histogram Noise Correction	45

LIST OF TABLES

3.1	PCC score between each selected target material and scene-extracted grass signature shown in Fig. 3.2.b.	14
3.2	Mathematical relationships used to compute target fill factor corresponding to Figure 3.3.	17
3.3	Hole pattern configurations for the four target-background mixture ratios.	17
5.1	PCC score between each target material spectrum and the mean scene-extracted grass signature from the L1, SMSR, CS, and NRL image cube.	32
5.2	Target Class SCR for each corrected image cube.	32
5.3	SCR of Target Classes With/Without Introduced Noise	37
5.4	Standard Deviation of Target Distributions	38
5.5	Distance between the Means of Target and Background Histogram Distributions	38

CHAPTER I

INTRODUCTION

Spatial nonuniformity, or fixed pattern noise (FPN), is a problem that affects nearly all focal plane array (FPA) sensors and is largely caused by manufacturing variability within each photodetector, resulting in each FPA pixel measuring the same incident radiation differently [1]. FPN degrades acquired imagery by superimposing a fixed noise pattern in the data over the imaged scene. In 2D staring camera imagery FPN gives the appearance that the scene was imaged through a dirty camera lens, whereas FPN appears as vertical striping artifacts in pushbroom sensor imagery. While FPN is known to particularly manifest in infrared sensors [2], it can also impact visible to short-wave infrared (VIS-SWIR) sensors, such as those commonly employed in hyperspectral imaging (HSI) systems.

FPN is usually compensated for through calibration procedures where a flat-field source is imaged by the camera at a range of precisely-controlled input radiances [3]. Despite careful calibration, residual nonuniformity is nearly always present in the calibrated data, largely for two reasons. First, detector responsivities are typically a nonlinear function of input radiance; however, pixels often are fabricated to have an approximately linear response within the expected operating range of the sensor. As such, response curves are commonly approximated by a linear model in order to account for the nonuniformity, which is clearly inaccurate in nonlinear regions [4]. Second, the detector responsivities slowly change with time due to a host of factors, such as the internal operating temperature of the camera electronics and the external environmental conditions of the sensor, such as temperature, air pressure, and humidity [1]. Fortunately, the drift is often slow enough that within a reasonable range of frames the pixel responsivities may be considered constant.

Common practice for removing FPN in HSI data cubes is to apply a linear two-point calibration, i.e., a pixel-wise gain and offset correction, where such calibrated data is often referred to as Level 1 (L1) calibrated data (along with any bad pixel correction). Often times, the gain map is carefully generated under laboratory conditions and later used in the field. The offset map is typically generated by imaging the camera shutter prior to each image scan or at the beginning of the data collection. This results in the offset estimates being recent while the gain map can be more subject to drift due to the time that has elapsed since its creation. This drift in the gain map results in calibration error, or residual fixed pattern noise (RFPN), and can have an adverse effect on the performance of detection, identification, and tracking tasks in HSI data. The only viable solution for estimating and removing RFPN is to apply strategies that can estimate FPN through exploiting scene properties inherent within the data. These strategies are known as scene-based nonuniformity correction (SBNUC) algorithms and attempt to estimate and remove any RFPN present in the data.

SBNUC algorithms predominantly have been designed for staring array imagery. These algorithms are primarily based upon statistical or frame-to-frame registration methods that work to estimate and eliminate RFPN. Statistical methods are often based upon the assumption that the spatial and temporal radiance distribution is identical across all pixels. Various statistical algorithms have been proposed, such as the Kalman-filtering based approach by Torres and Hayat [5], the least mean squares (LMS) neural network approach by Scribner *et al.* [6], the gated LMS approach by Hardie *et al.* [7], and the constant-statistics (CS) approach by Harris *et al.* [8]. Registration-based methods utilize frame-to-frame motion to cancel the scene content via image registration, leaving only FPN terms that can be estimated. The frame-to-frame shift can be whole pixel or subpixel. Various registration

algorithms have been introduced, such as the family of subpixel algebraic SBNUC techniques by Ratliff *et al.* [9, 10, 11], subpixel offset unification approach by Black and Tyo [12], scene cancellation subpixel approach by Zuo [13], and two full pixel registration-based approaches by Hardie *et al.* [14] and O’Neil [15].

We focus our attention in this work on the correction of FPN in HSI systems. HSI systems rely on the same FPA sensors; however, the optical system contains a dispersive element that converts one spatial dimension into a spectral dimension. The second spatial dimension is then built up over time and these types of sensors are known as pushbroom sensors. A number of SBNUC algorithms for pushbroom sensors are in the literature, namely, the sorted mean spatial ratio (SMSR) technique by Ratliff and Kaufman [16], the Naval Research Laboratory’s (NRL) mean spatial ratio method by Leathers *et al.* [17], the low-dimensional destriping procedure by Adler-Golden *et al.* [18], total variation approach by Yuan *et al.* [19], an energy minimization via regularization approach by Bouali [20], a neural network approach by Meza [21], and a high dimensional subspace approach by Acito *et al.* [22].

Within the HSI community, application of SBNUC algorithms has been met with mixed opinions as to how beneficial they can be. In some cases, significant improvement to target detection can be obtained, while in others little to no improvement (or even worsened performance) is observed. The goal of this work is to first investigate the effect that RFPN has upon target detection performance. Then, SBNUC algorithms will be applied to appropriate data to better understand their performance. This has traditionally been a difficult task to undertake due to limited data being available for such a study. To support such an investigation, we conducted a data collection experiment with a SWIR HSI sensor using material target panels designed specifically for this study. The targets were created using materials

that have different degrees of inherent separability from natural grass backgrounds. Furthermore, the targets were created to produce different target-background mixture levels in order to yield high fidelity receiver operating characteristic (ROC) curves. The reason for creating such targets is to determine how target detection performance is affected as a function of RFPN and inherent target-background separability. Moreover, our goal is to study the performance of SBNUC algorithms commonly used in the HSI community. Hence, in this thesis we apply several SBNUC algorithms and study their ability to remove RFPN and furthermore the effect this has on target detection performance. The specific algorithms we examine in this work are the CS [8], SMSR [16], and NRL [17] approaches.

This thesis is organized as follows. Our sensor model development and a description of the SBNUC algorithms we apply are presented in Chapter II. Data collection planning and target design are discussed in Chapter III. Chapter IV describes all data processing, exploitation, and RFPN simulation. Target detection results and all relevant discussion are presented in Chapter V. Finally, conclusions are stated in Chapter VI.

CHAPTER II

SENSOR MODELING & SBNUC APPROACH

2.1 Sensor Model

In a pushbroom sensor, the FPA acquires spatial information along one dimension and spectral information along the other due to the presence of dispersive optics in the imaging system. A three-dimensional hyperspectral data cube can then be obtained by scanning the sensor across the scene to build up the second spatial dimension. This results in a hyperspectral image cube of dimensions $S \times B \times L$, where S is the number of cross-track spatial samples, B represents the number of discrete band (or wavelength) images, and L represents the number of along-track spatial lines that are collected across time. This can be seen in Figure 2.1.

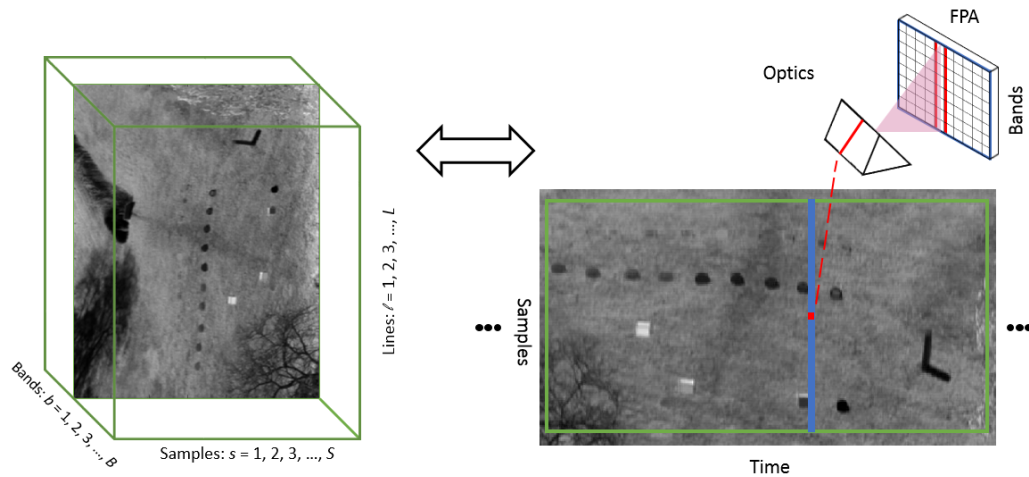


Figure 2.1: A hyperspectral sensor scanning over a target array and an example of its corresponding hyperspectral image cube.

As described above, the responsivity of each pixel in the FPA can be nonlinear and furthermore slowly change with time. It is common practice to assume a linear detector model since often detectors are fabricated to have an approximately linear response in the expected operating range of the sensor [1, 3]. As such, we first assume a linear detector model and second we assume that the drift in the detector responsivity is slow enough to be negligible within the time it takes to collect an image cube. Our detector model is then

$$y(s, b, l) = g(s, b) \cdot x(s, b, l) + o(s, b) + \eta(s, b, l), \quad (2.1)$$

where $x(s, b, l)$ is the input radiance at time l , $g(s, b)$ and $o(s, b)$ are the pixel's gain and offset, respectively, and $y(s, b, l)$ is the pixel output in digital counts at time l . $\eta(s, b, l)$ is frame-to-frame temporal sensor noise and is assumed to be independently distributed zero-mean Gaussian noise. Due to the averaging mechanisms present across the correction algorithms we largely ignore the effects of temporal noise since it becomes negligible.

FPN results due to each pixel's gain and offset being different, giving rise to the nonuniformity. One common method of removing FPN is to apply a linear two-point calibration. This two-point calibration, otherwise known as a Level 1 (L1) calibration, is defined by placing a calibrated flat-field source at a known radiance in front of the camera system, exposing each pixel to the same radiance level. Two flat-field radiance levels, x_1 and x_2 , are used in this case. Once acquired, the data can be used to estimate the gain and offset for each detector according to

$$\hat{g}(s, b) = \frac{y_2(s, b, l) - y_1(s, b, l)}{x_2 - x_1}, \quad (2.2)$$

and

$$\hat{o}(s, b) = y_1(s, b, l) - \hat{g}(s, b)x_1. \quad (2.3)$$

These gain and offset estimates are then applied to correct for the nonuniformity in each pixel (producing the L1 image) according to

$$\hat{x}(s, b, l) = \frac{y(s, b, l) - \hat{o}(s, b)}{\hat{g}(s, b)} = \frac{g(s, b) \cdot x(s, b, l) + o(s, b) - \hat{o}(s, b)}{\hat{g}(s, b)}. \quad (2.4)$$

Typically, this calibration results in the data being converted from units of digital counts to a desired radiometric unit. We assume that the calibration unit is radiance for the remainder of this work.

It is worth noting that often times in practice the camera shutter is the only flat-field source available at the time of collection. It is used to collect a “dark” frame (i.e., 0 input radiance) while relying on an estimate of the gain map that was acquired previously in time. Clearly then, this scenario is more prone to error in the gain estimates and contributes to RFPN. Due to this common situation, here we assume that all RFPN may be attributed to gain nonuniformity, i.e., we assume that $o(s, b) = 0 \quad \forall s, b \in \mathbb{Z}^+$. Therefore, the sensor model reduces to

$$\hat{x}(s, b, l) = \frac{g(s, b) \cdot x(s, b, l)}{\hat{g}(s, b)} = g_r(s, b) \cdot x(s, b, l), \quad (2.5)$$

where $g_r(s, b) = \frac{g(s, b)}{\hat{g}(s, b)}$ represents the residual gain nonuniformity present after L1 calibration (where each residual gain is assumed to be close to 1) and is the source of RFPN that we study.

2.2 Algorithm Descriptions

We implement and apply three specific SBNUC algorithms from the literature in this work. In particular, we investigate the CS [8], SMSR [16], and NRL [17] algorithms. The CS algorithm attempts to remove RFPN by normalizing each pixel response to have the same mean and standard deviation over time. These quantities are estimated for each pixel

using data from the image cube along the line (temporal) dimension, i.e.,

$$\mu_{cs}(s, b) = \frac{1}{L} \sum_{k=1}^L \hat{x}(s, b, l) \quad (2.6)$$

and

$$\sigma_{cs}(s, b) = \sqrt{\frac{\sum_{k=1}^L (x(s, b, l) - \mu_{cs}(s, b))^2}{L}}. \quad (2.7)$$

These estimates are then applied to correct each L1 image value according to

$$\hat{\hat{x}}(s, b, l) = \frac{(\hat{x}(s, b, l) - \mu_{cs}(s, b))}{\sigma_{cs}(s, b)}. \quad (2.8)$$

In order for the CS algorithm to produce reliable estimates of the mean and standard deviation that each pixel must observe the same distribution of scene radiance over time. This rarely happens in practice and typically requires a large number of image frames to satisfy the statistical assumptions (often $> 10,000$). When not enough samples are available in the data cube severe ghosting artifacts can be present after correction.

The SMSR algorithm also takes a statistical approach, but incorporates inherent mechanisms to mitigate adverse artifacts in the corrected data. The algorithm first sorts the image cube according to radiance value along the line (temporal) dimension. This helps to ensure that neighboring pixels have similar scene values. Then, within each band image, neighboring columns within this sorted image are ratioed. Ratioing begins at the central column and emanates outward towards the edges of the image. The sorted and ratioed image takes the form,

$$\gamma(s, b, l) = \begin{cases} \frac{\hat{x}(s+1, b, l)}{\hat{x}(s, b, l)} \approx \frac{g_r(s+1, b)}{g_r(s, b)}, & s > c \\ 1, & s = c \\ \frac{\hat{x}(s-1, b, l)}{\hat{x}(s, b, l)} \approx \frac{g_r(s-1, b)}{g_r(s, b)}, & s < c \end{cases} \quad (2.9)$$

where c indicates the starting column of a given band image (often chosen to be the central pixel). The ratios are further sorted along the time dimension a second time, causing outlier

values to move to the beginning and end of each column. A percentage of these outliers are excluded and the resulting gain ratio estimates are averaged. At this stage, the ratio estimates will only unify a given pixel to that of its adjacent neighbor. To convert it into a more useful form that will unify the gains across the entire image to a common value, a cumulative product is applied such that

$$\Gamma(s, b) = \begin{cases} \prod_{q=s}^c \hat{\gamma}_{q,b}, & s < c \\ 1, & s = c \\ \prod_{q=c}^s \hat{\gamma}_{q,b}, & s > c \end{cases}, \quad (2.10)$$

where $\hat{\gamma}$ corresponds to gain ratios estimates excluding outliers. Then, the final gain correction matrix is of the desired form:

$$\Gamma \approx \begin{bmatrix} \frac{g_r(c,1)}{g_r(1,1)} & \cdots & \frac{g_r(c,1)}{g_r(c-1,1)} & 1 & \frac{g_r(c,1)}{g_r(c+1,1)} & \cdots & \frac{g_r(c,1)}{g_r(s,1)} \\ \frac{g_r(c,2)}{g_r(1,2)} & \cdots & \frac{g_r(c,2)}{g_r(c-1,2)} & 1 & \frac{g_r(c,2)}{g_r(c+1,2)} & \cdots & \frac{g_r(c,2)}{g_r(s,2)} \\ \vdots & \cdots & \vdots & \vdots & \vdots & \cdots & \vdots \\ \frac{g_r(c,b)}{g_r(1,b)} & \cdots & \frac{g_r(c,b)}{g_r(c-1,b)} & 1 & \frac{g_r(c,b)}{g_r(c+1,b)} & \cdots & \frac{g_r(c,b)}{g_r(s,b)} \end{bmatrix}. \quad (2.11)$$

When this gain correction matrix is multiplied with a given L1 band image, notice that it will remove the respective gain and multiply it with the gain of the central pixel, effectively synchronizing the RFPN. It was additionally shown in [16] that further improvement could be obtained by applying this approach in the principal component (PC) domain. Thus, a principal components transform (PCT) is first applied to the L1 image cube, the SMSR algorithm is then applied as described above in PC space, and then finally inverse transformed back into radiance space.

The NRL algorithm is based upon similar mechanisms as the SMSR technique, namely that it computes the ratios of samples in adjacent columns. However, rather than performing any sorting or averaging operations, the median value of the computed ratios within each column is used. A cumulative product is similarly performed on these median ratio values to obtain a similar form to the correction matrix of the SMSR algorithm. The NRL algorithm is illustrated in Figure 2.2.

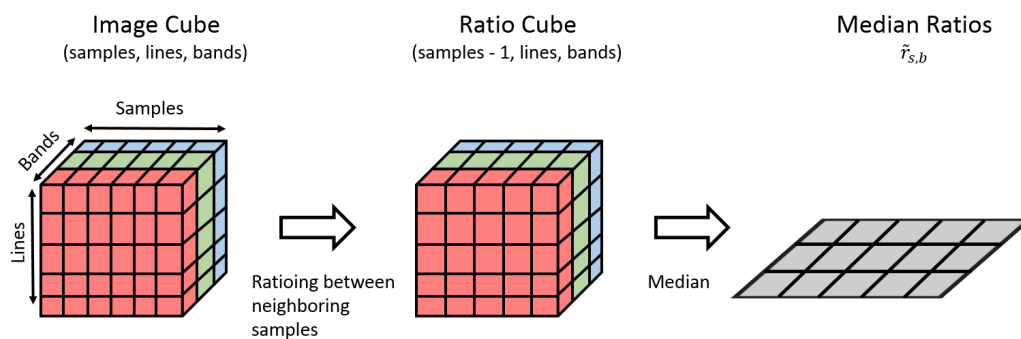


Figure 2.2: Procedural drawing of the mean spatial ratio (NRL) algorithm.

CHAPTER III

DATA COLLECTION PLANNING

Our overall objective in this study is to better understand the effect that RFPN has upon HSI target detection performance for target materials which have different levels of inherent separability from the background (or non-target materials). In particular, we want to understand how the presence of RFPN affects targets that are difficult to detect (low background separability), easy to detect (high background separability), and those that are in between these two extremes (moderate background separability). The hypothesis is that RFPN will not significantly affect target detection performance of low and high separable materials as much as moderately separable materials. This concept is illustrated on the left axes in Fig. 3.1 where simple Gaussian distributions are used to represent the target and background distributions. When an SBNUC algorithm is applied to the data, the width of the distributions are expected to decrease, as illustrated at right in Fig. 3.1. When this occurs notice that materials that have low separability remain unseparable from the background distribution. Materials which have high separability remain separable despite the decrease in RFPN. Finally, moderately separable material's detectability will be most impacted as they will overlap less with the background distribution after SBNUC.

One goal was to demonstrate these trends using real HSI data; however, no real data was available to support such an investigation. Thus, we designed and conducted an experiment specifically for this study. We selected target materials with inherent levels of separation from natural backgrounds to provide a range of difficulty in their detectability. Furthermore, we constructed targets to precisely control the level of mixture between each target material and the background to allow for high sampling of the resulting ROC detection curves. The

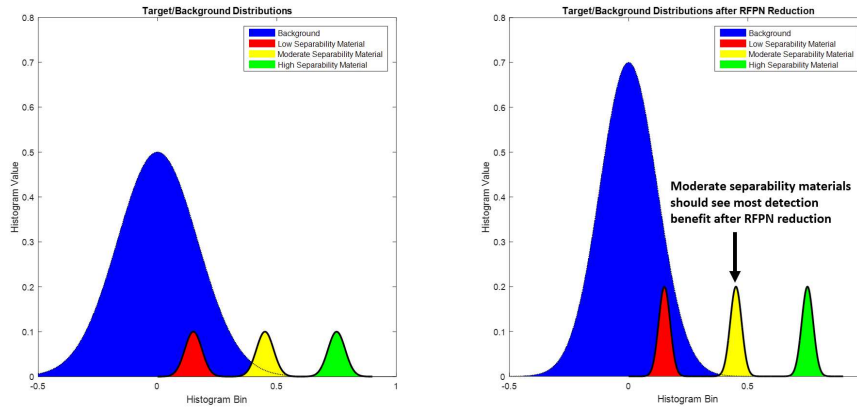


Figure 3.1: Illustration of distributions for materials of different degrees of inherent background separability before and after RFPN reduction: low separability materials remain difficult to detect even after RFPN removal, high separability materials are detectable independent of RFPN, and moderately separable materials become more detectable after RFPN removal and thus see the most benefit in improved detectability.

details of material selection and target design, as well as the data collection scenarios are discussed in the following subsections.

3.1 Material Selection

A key component of this data collection was selecting appropriate target materials having differing levels of inherent separability from anticipated natural backgrounds. A study was conducted to identify such materials based on their relative reflectance spectra with the added constraints that they be easily obtainable and conducive to target construction. The material separability study was conducted using material libraries provided by the Air Force Research Laboratory containing both man-made and natural materials (891 signatures in total). Representative grass background signatures were extracted from calibrated data previously collected with the same SWIR HSI sensor under similar atmospheric conditions anticipated for the data collection. These signatures were used to generate appropriate background statistics for computing separability measures between the background distribution and each material library signature. While several separability measures were considered, Pearson’s Correlation Coefficient (PCC) was ultimately chosen for final material selections, defined as

$$\rho_{TB} = \frac{E[(\mathbf{T} - E[\mathbf{T}])(\mathbf{B} - E[\mathbf{B}])]}{\sigma_{\mathbf{T}}\sigma_{\mathbf{B}}}, \quad (3.1)$$

where \mathbf{T} and \mathbf{B} indicate the target and background signatures, respectively, $E[\cdot]$ is the expected value operator, and $\sigma_{\mathbf{T}}$ and $\sigma_{\mathbf{B}}$ are the spectral standard deviations of the target and background signatures, respectively.

We obtained PCC scores for each signature in the material library against the scene-extracted background reflectance signature. We selected four target materials for use in the study: a mixture of fine domestic American hardwood sawdust (low separability); Valspar Signature Matte Tan Latex Paint (moderate separability); fine white craft sand (moderate

separability); and red Plasti-Dip[®] rubberized paint (high separability). These materials spanned a wide range of inherent separabilities from our mean background signature. We purchased these materials and applied them to small aluminum test panels. We then performed laboratory spectrometer contact measurements to obtain reflectance signatures for each target material. The PCC score was then computed between each test panel material measurement and the average scene-extracted grass background signature and are shown in Table 3.1. A photo of these commercially-available materials along with their associated measured reflectance spectra are displayed in Fig. 3.2. As discussed in more detail in

Table 3.1: PCC score between each selected target material and scene-extracted grass signature shown in Fig. 3.2.b.

Target Class	PCC Score
Sawdust	0.9466
Sand	0.7858
Tan Latex	0.7917
Red Plasti-Dip [®]	0.0191

the next subsection, the targets were created from circular aluminum panels. The materials were applied to these aluminum panels by first applying a Krylon Matte Deep Gray Paint+Primer. Then, the Plasti-Dip[®] and tan latex paint were applied directly to the gray primered panels. The sawdust and sand were adhered to the gray primered panels by first applying 3M Multipurpose Super 77 Spray Adhesive. This was performed three times to ensure that the targets were well-covered by the fine particulate materials. Additionally, we created a target panel and applied Krylon Matte Black Paint to be used as a 0% reflectance calibration target.

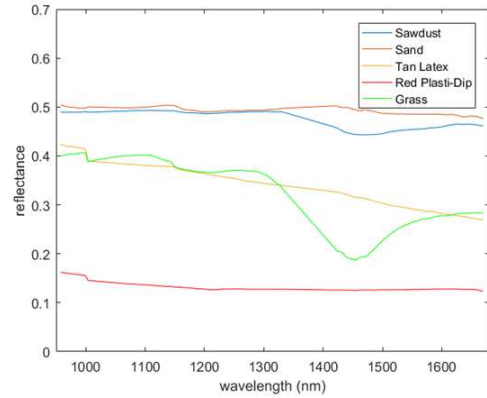


Figure 3.2: Selected materials used for target creation are shown at left with their corresponding spectral signatures plotted at right, sampled to the appropriate sensor wavelengths. Shown for reference is the average scene-extracted grass background signature used in the target separability study.

3.2 Target Mixture Simulation & Fabrication

A secondary goal of target design was to create targets that introduce controlled levels of mixing between the selected target materials and the natural background (we chose target-background mixture ratios of 100%, 80%, 60%, 40%, and 20%). In order to construct a well-defined ROC curve, numerous samples are needed at each mixture level, where the number of pixels should be greater than 10 divided by the false alarm probability [23]. Therefore, for the most stringent case of an 20% target-background mixture ratio, a minimum of 50 pixels are needed.

The targets were created from 0.080" thick circular aluminum panels that are 30" in diameter. For each of the four target materials, sets of five targets were created (for a total of 20), one at each of the five target-background mixture ratios (100%, 80%, 60%, 40%, and 20%). The mixture levels were created by punching holes (using a hydraulic CNC turret

press) of various shapes and sizes in the central 24" × 24" region of each aluminum panel. A simulation was developed in order to determine the optimal hole shape, size, and spacing to achieve a given mixture ratio at a specified camera ground sample distance (GSD). The idea was to create hole patterns that are unresolvable at the given GSD of 1.5 inches so that uniform mixing is achieved in the final measured images. Each mixture level thus required a different hole pattern be created and we were constrained to a discrete set of circular and square hole punches of various sizes available at the fabrication facility.

Figure 3.3 shows square target regions with inset circular and square hole patterns that are used to develop the mathematical relationships used to compute a given target-background mixture level, as displayed in Table 3.2. Here, f represents the target fill factor, L_t is the length of the side of the square target area, L_h is the length of the side of the square hole punch, and D_h is the diameter of the circular hole punch. The simulation was created in MATLAB where the target and hole mixture patterns were created as a high resolution binary image (target pixels were set to 1 and background pixels set to 0). Each binary image was then convolved with a point spread function matching the sensor and then decimated according to the desired GSD expected in the experiment. The values of the mixed pixels in these output images then gives the approximate mixture level expected for the given hole pattern configuration. Table 3.3 shows the hole pattern shapes, sizes, and spacing that were used to create the actual targets. The simulated high resolution binary images corresponding to these parameters are displayed in Fig. 3.4.a and the simulated sensor-sampled images are shown in Fig. 3.4.b for an example sensor GSD of 1.5 inches.

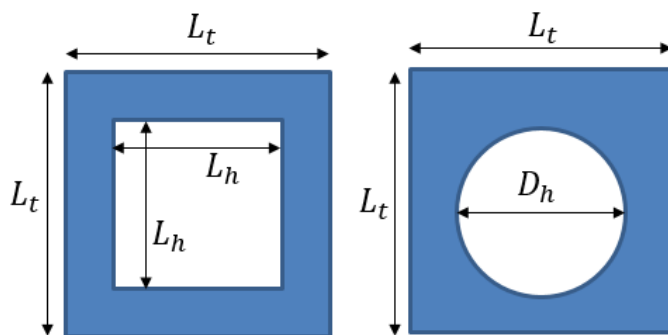


Figure 3.3: Square and circular hole-punch guides created for the target mixture simulation.

Table 3.2: Mathematical relationships used to compute target fill factor corresponding to Figure 3.3.

Square Punch	Circular Punch
$f = (\frac{L_h}{L_t})^2$	$f = \pi(\frac{D_h}{2L_t})^2$
$L_t = \frac{L_h}{\sqrt{f}}$	$L_t = \frac{D_h}{2} \sqrt{\frac{\pi}{f}}$
$L_h = L_t\sqrt{f}$	$D_h = 2L_t\sqrt{\frac{f}{\pi}}$

Table 3.3: Hole pattern configurations for the four target-background mixture ratios.

Target-Background Mixture Level	Hole Shape	Hole Size	Hole Spacing	Alternating Row Offset
80%	Circular	0.25" D	0.5"	0.25"
60%	Circular	0.344" D	0.5"	0.25"
40%	Circular	0.437" D	0.5"	0.25"
20%	Square	0.75"	0.85"	0.425"

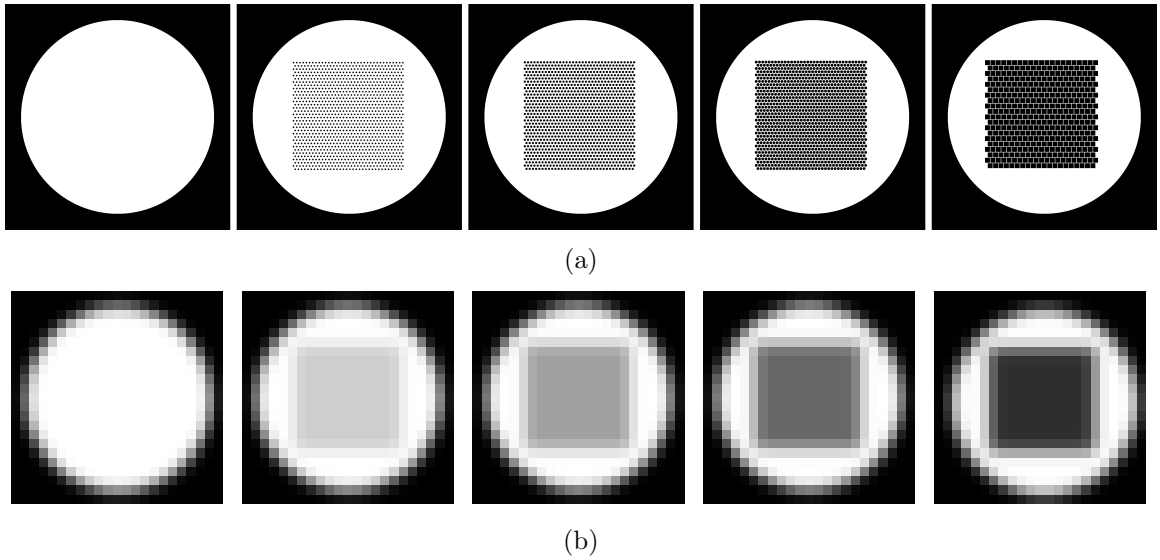


Figure 3.4: Mixture target simulated images using the hole pattern configurations from Table 3.3. a) shows the high resolution binary target images (from left to right) at target-background mixture levels of 100%, 80%, 60%, 40%, and 20%. b) shows the corresponding sampled images after passing through a simple optics model and sampled at a GSD of 1.5 inches. The central region estimated mixture ratios are (from left to right) 100%, 79.97%, 62.62%, 37.91%, and 18.18%.

3.3 Collection Scenario and Conditions

The data collection was performed in Dayton, OH during November, 2018. Light cloud cover and low/parallel sun angles to the target surface included variable illumination conditions throughout the collection. To address these illumination conditions, three target scenarios were created by orienting the targets at three different angles (out of plane) relative to the sensor. The sensor was positioned in a tower with an angle of depression of 20° . In the first target scenario, the targets were positioned at nadir to the sensor at an angle of elevation of 70° from the ground. In the second scenario the targets were repositioned to an angle of elevation of 45° relative to the ground, and finally at a 10° angle of elevation relative to the ground in the third scenario. Figure 3.5 shows an illustration of target placement in the scene for each scenario. Visible-band ground truth images of each target scenario taken from the tower vantage point are shown in Figure 3.6. Standoff relative reflectance signatures were measured at the beginning of each scenario using Malvern Panalytical's ASD FieldSpec[®] spectrometer for all material and calibration targets, as well as for numerous regions of the grass background. Figure 3.7 displays various ground truth images from the data collection experiment of the target array taken from the ground and collection tower.

A single band image can be seen from each scenario in Figure 3.8. The collection sensor and acquisition computer both experienced a number of issues during the data collection that resulted in intermittent temporal artifacts, interlacing issues, and dropped frames. Furthermore, the sun angle for Scenarios 1 and 2 resulted in sub-optimal illumination conditions for the target array. The target panel shadows in the ground truth images reveal that the sun angle is oriented orthogonal to the target array and resulted in some of the target panels not being well-illuminated (simply a consequence of the time of year). This

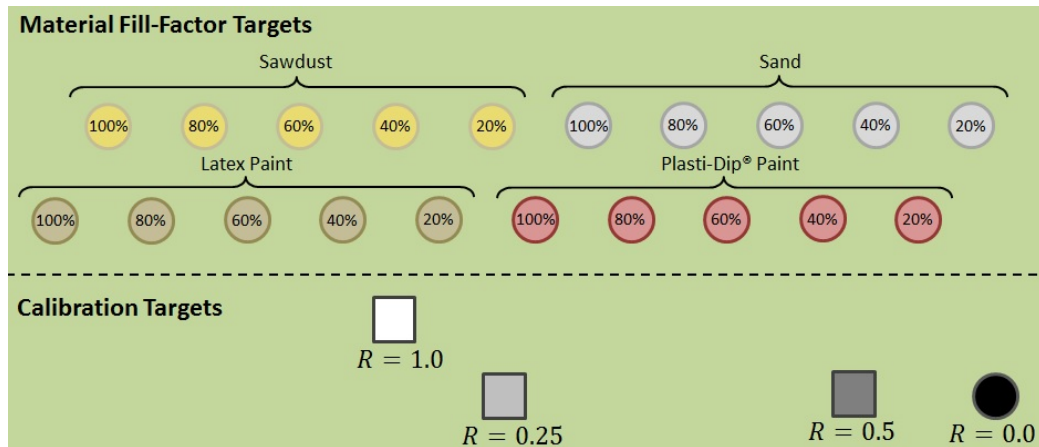


Figure 3.5: Target array layout for each scenario.

is unfortunate since the targets were designed to have the indicated mixture ratios when viewed at nadir. In Scenario 3, however, the target panels are all well-illuminated and all clouds had dissipated by this time. For this reason we focus on data sets from Scenario 3 for the remainder of this study.



Figure 3.6: Imagery collected from the data collection. The top image depicts Scenario 1 of the target array where each target is orientated with angles of elevation relative to the ground of 70° . The middle image depicts Scenario 2 where each target is orientated with angles of elevation relative to the ground of 45° , and the bottom image depicts Scenario 3 where each target is orientated with angles of elevation relative to the ground of 10° .



Figure 3.7: Imagery collected from the data collection. The top image depicts Scenario 1 of the target array. The middle image shows the viewpoint behind the target array looking up towards the tower. The bottom image shows the sensor as well as the target array.

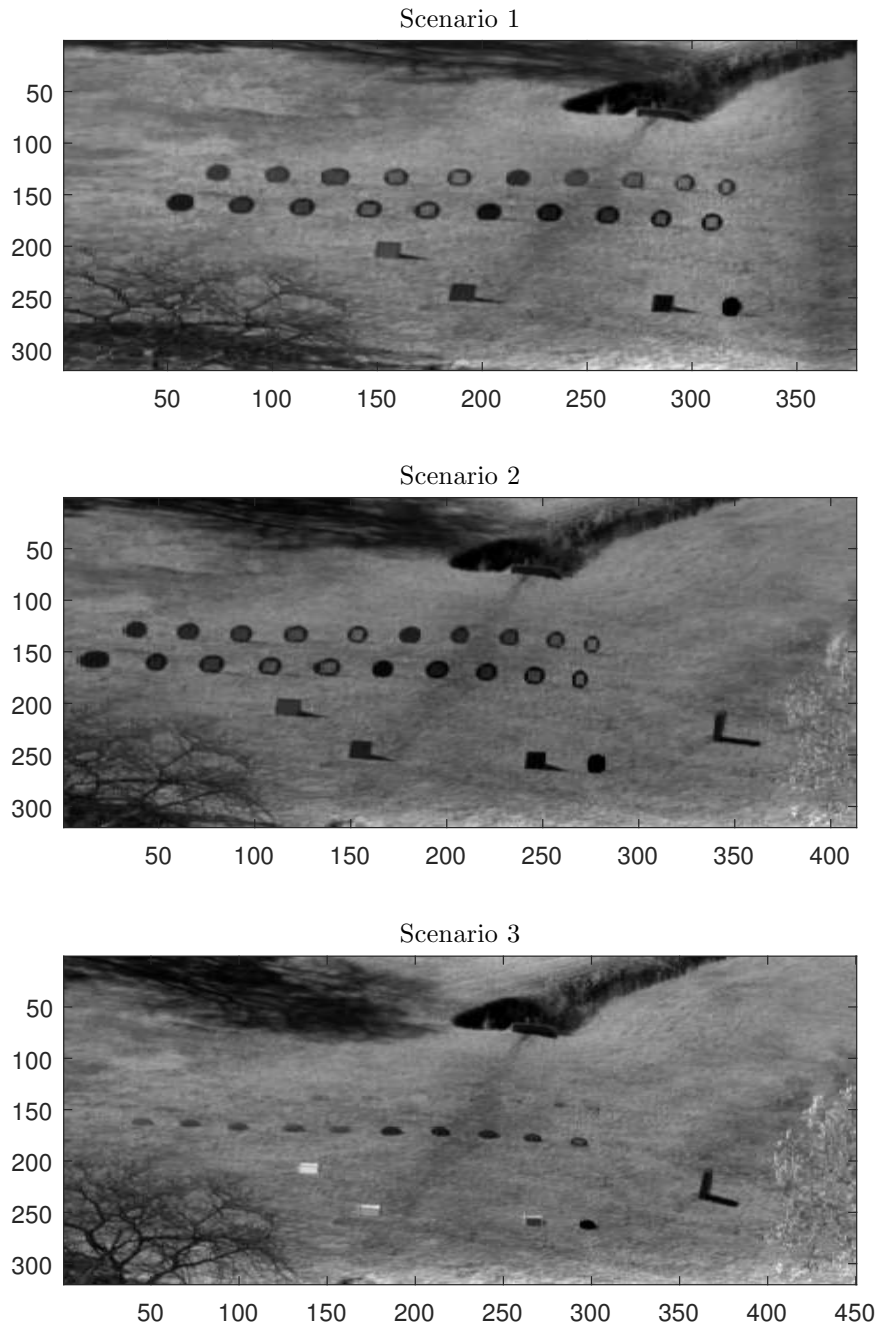


Figure 3.8: Band 25 image from the data cube in Scenario 1 is shown on top, Scenario 2 is shown in the middle, and Scenario 3 is shown on the bottom (The calibration and processing of the data is discussed in Chapter IV).

CHAPTER IV

DATA PROCESSING & EXPLOITATION

The HSI sensor used in this experiment has a 320×256 SWIR-based FPA sensor. In each data set, the sensor was slewed across the scene and collected 450 lines. This resulted in HSI image cubes of size 320 samples \times 450 lines \times 256 bands over a wavelength region of 900 to 1600 microns. Prior to each collection scenario, flat-field imagery was collected using the camera shutter (for offset correction) and a flat-field Labsphere[®] integrating sphere was imaged at mid- and high-luminance levels for calibration purposes. Bad pixel correction was enabled in the sensor acquisition software and thus is inherent to the collected data.

Each raw data cube was calibrated into an L1 data cube using a two-point calibration procedure [3]. The shuttered and high luminance data were used in the calibration. The shutter and Labsphere[®] luminance levels were converted to spectral radiance at each sensor wavelength and a separate gain and offset vector was computed and applied to each band image. Atmospheric bands were then removed from the data so that only band corresponding to wavelengths of 950-1108, 1137-1331, and 1423-1669 microns were used. Atmospheric compensation was performed to convert the L1 data cube from radiance into reflectance using a multi-point empirical line method (ELM) [24]. The pixels corresponding to each of the four calibration panels (as shown in Figure 3.5) in the scene were extracted and a piecewise linear 4-point ELM was performed. The SBNUC algorithms mentioned above, namely the SMSR [16], NRL [17], and CS [8] algorithms, were then applied to each L1 image cube to further reduce RFPN. It is important to note that these algorithms are applied to the L1 data in radiance units and the ELM is further performed on each of these corrected cubes to convert the data to relative reflectance before any detection assessment is performed.

The top row of Fig. 4.1 displays the 25th band image from the L1 calibrated data cube, the SMSR SBNUC-applied L1 cube, the CS SBNUC-applied L1 image cube, and the NRL SBNUC-applied L1 image cube. The L1, SMSR, and NRL resulting band images look similar whereas some artifacts can be observed in the CS result near the top and central portions of the image. RX anomaly detection [25] results, or maps, are useful for visually assessing RFPN present in HSI image cubes. Each value of the RX map is computed according to

$$\text{RX}(\mathbf{x}) = (\mathbf{x} - \mu_x)^T \cdot \mathbf{\Gamma}^{-1} \cdot (\mathbf{x} - \mu_x), \quad (4.1)$$

where $(\mathbf{x} - \mu_x)^T$ is any mean-subtracted scene signature and $\mathbf{\Gamma}$ is the covariance matrix computed from the entire scene. The RX detection map for each image cube is displayed in the second column corresponding its respective data cube. In the L1 results, there is a reasonable amount of RFPN that manifests as interlaced striping artifacts across the RX map. These artifacts have largely been removed after application of the SMSR algorithm. The NRL algorithm reduces the striping artifacts slightly, but they are still noticeable after correction. Furthermore, it appears to introduce some dark banding artifacts that can be observed near the top of the RX image. The CS algorithm shows extreme artifacts across several regions of the scene. These artifacts are present because the CS algorithm assumes that the temporal intensity distribution of each line in the scene is identical. In areas where only grass is observed, not enough intensity diversity is present and thus yield severe “burn-in” artifacts. Typically, thousands of samples are needed for this algorithm to obtain reasonable results—we included it in this work due to its common use in practice. Truth masks were created for both target and background grass pixels and are shown in Figure 4.2. The truth masks were categorized according to each target material class and further sub-categorized according to each target mixture level. Each of the four calibration panels in the scene were also labeled separately in the truth mask to support the ELM atmospheric

correction. It is important to note that we limit the background signatures to those of grass pixels since our initial material selections were based upon separability from scene-extracted grass pixels.

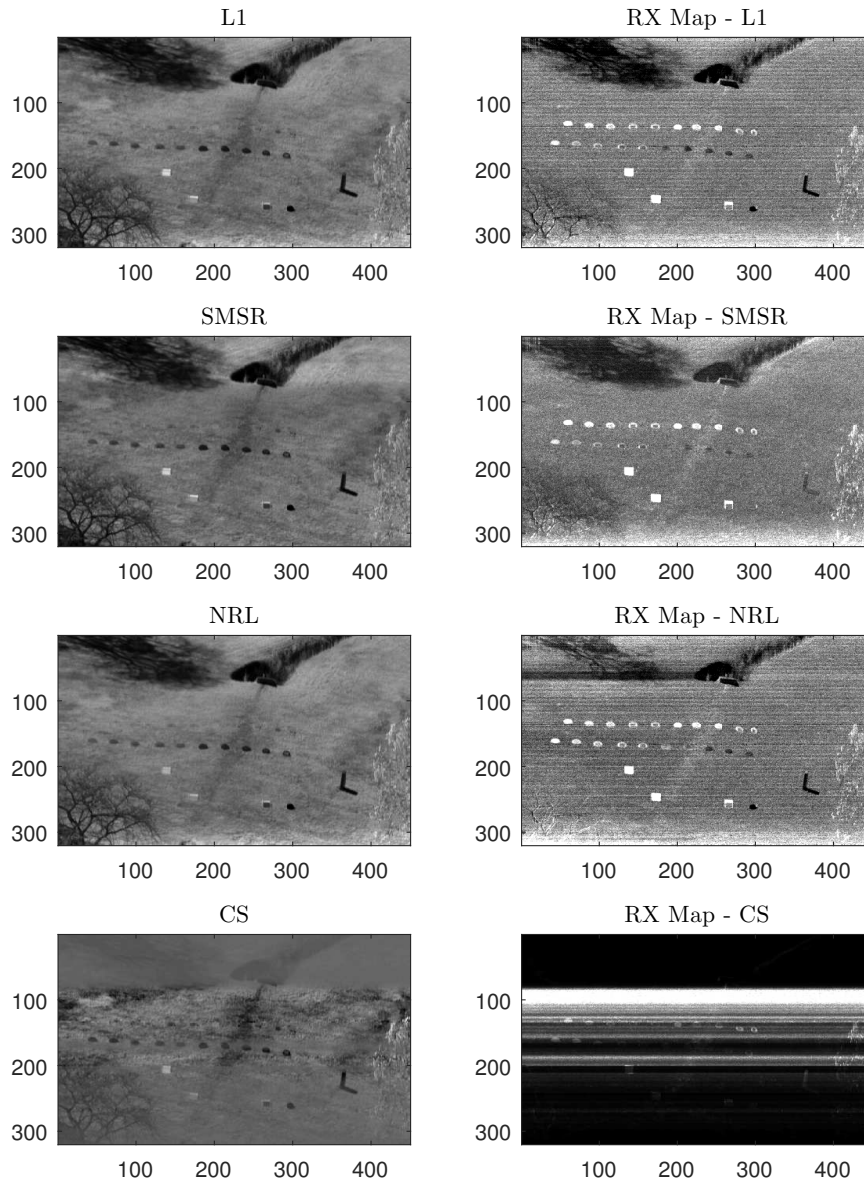


Figure 4.1: The left column shows the band 25 image from the data cube after L1 calibration, SMSR, NRL, and CS SBNUC algorithms. The right column shows the resulting RX map for the corresponding image cube at left.

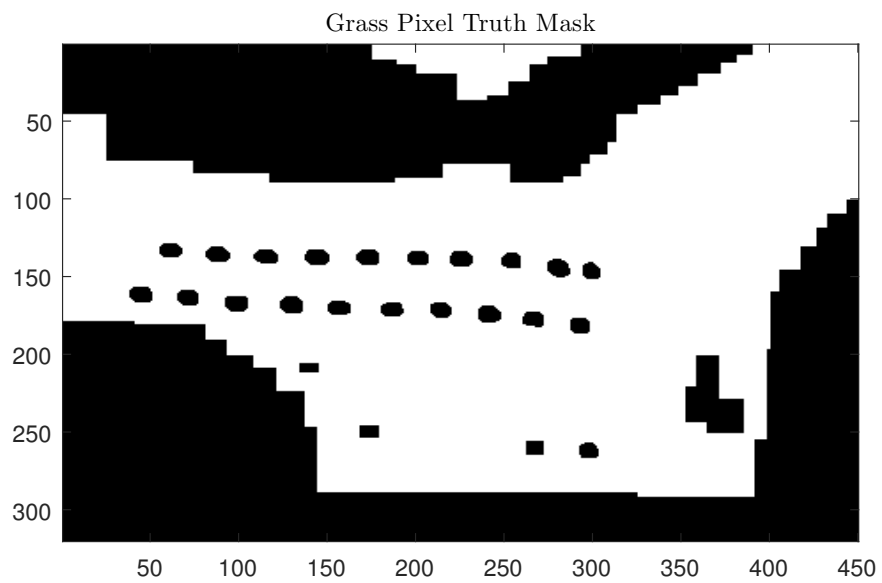
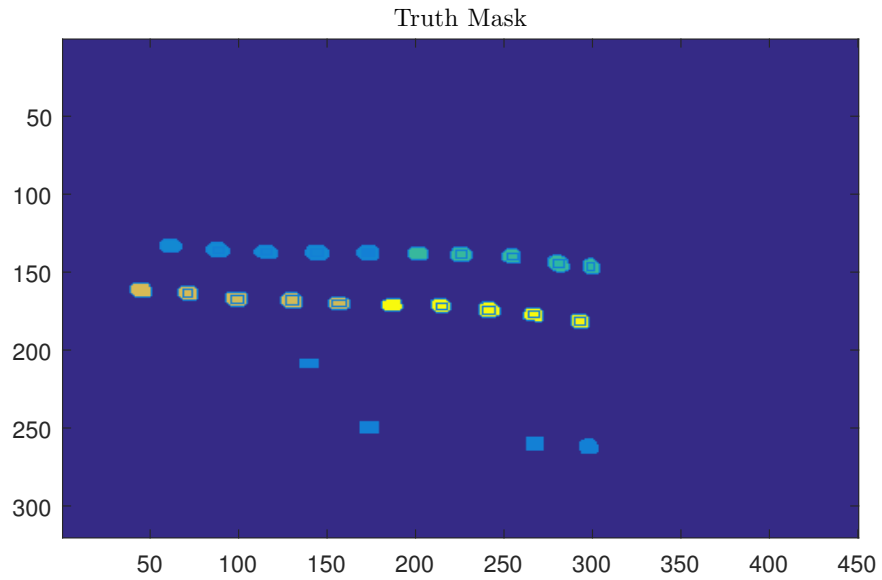


Figure 4.2: The created truth mask showing all target materials and mixture regions and calibration target panels is shown at top. The background truth mask consisting of grass-only pixels is shown at bottom.

CHAPTER V

DETECTION PERFORMANCE

To evaluate the detection performance of each target material, we use the adaptive cosine estimator (ACE) algorithm [26] to compute a detection score for each pixel location using a given ELM-corrected data cube and the various target reflectance signatures measured in-field with the ASD field spectrometer (we used spectra from the 100% target material panel). The resulting ACE maps were then evaluated in conjunction with the truth mask for a given target material class and the grass background pixels to produce a ROC curve. Here, we study the effect RFPN has upon target-background separability. The ACE algorithm computes the cosine of the angle between a given scene signature and specified target signature in whitened space. The ACE score between two such signatures is thus computed according to

$$\text{ACE}(\mathbf{x}, \mathbf{s}) = \frac{\tilde{\mathbf{x}} \cdot \tilde{\mathbf{s}}^T}{|\tilde{\mathbf{x}}| \cdot |\tilde{\mathbf{s}}|}, \quad (5.1)$$

where $\tilde{\mathbf{x}} = \mathbf{\Gamma}^{-\frac{1}{2}}(\mathbf{x} - \mu_X)$ is any whitened scene signature and $\tilde{\mathbf{s}} = \mathbf{\Gamma}^{-\frac{1}{2}}(\mathbf{s} - \mu_X)$ is the whitened target signature. μ_X and $\mathbf{\Gamma}$ are the mean and covariance matrix computed across all scene-extracted grass spectra and $|\tilde{\mathbf{x}}|$ and $|\tilde{\mathbf{s}}|$ are the magnitudes of the whitened scene and target signatures, respectively.

To provide additional assessments of separability, we compute the signal-to-noise ratio (SNR) according to

$$\text{SNR} = \frac{\sigma_{\text{ACE}(\mathbf{X}, \mathbf{s})}}{\sigma_{\text{ACE}(\mathbf{X} + \mathbf{N}, \mathbf{s})}}, \quad (5.2)$$

where $\sigma_{\text{ACE}(\mathbf{X}, \mathbf{s})}$ and $\sigma_{\text{ACE}(\mathbf{X} + \mathbf{N}, \mathbf{s})}$ are the standard deviations of the ACE scores before and after introduced noise, respectively. If we included all background pixels (i.e., non-grass)

for computing the spectral mean and covariance, we would expect detection performance to decrease. We define the median signal-to-clutter ratio (SCR) as

$$\text{SCR}(\mathbf{T}, \mathbf{B}) = \frac{\text{median}\{ACE(\mathbf{T}, \mathbf{s}) - \mu_{\mathbf{B}}\}}{\sigma_{ACE(\mathbf{B}, \mathbf{s})}}, \quad (5.3)$$

where \mathbf{T} indicates all signatures for a given target class and \mathbf{B} are all signatures from the grass background class. $\mu_{\mathbf{B}}$ is calculated similarly to that of Equation 2.6 using background signatures.

We first evaluated detection performance of the target materials using the L1, SMSR, NRL, and CS corrected data sets displayed in Fig. 4.1. We then introduced gain-based RFPN into the data and study the effect that RFPN has upon detection performance.

5.1 Detection Performance on Collected Data

ROC curves for each target material class resulting from each corrected image cube are displayed in Fig. 5.1. For each material, application of the SMSR algorithm shows an improvement in detection performance over the L1 image cube. The NRL algorithm results show a marginal improvement in detection performance for sawdust and sand while a decrease in performance for tan latex and the rubberized paint. The results from applying the CS algorithm show a substantial decrease in detection performance in all cases except for the Plasti-Dip[®] material. These results are consistent with the RX detection maps from Fig. 4.1. These same ROC curves are plotted in Fig. 5.2 grouped according to each corrected cube. In the L1 and SMSR cases, Plasti-Dip[®] is the most detectable, followed by tan latex paint, white sand, and finally sawdust. This is in line with the PCC separability predicted in Table 3.1. The PCC scores were again computed between the mean grass background pixel and each target material signature and are displayed in Table 5.1 for each corrected cube. We observe that the PCC scores computed from the L1 image cube vary

from those predicted by the initial material selection study. We attribute this in part to the grass background signatures that were used in the initial study were collected during a different time of year. In general, though, this indicates that the PCC scores generally correlate with the ROC results.

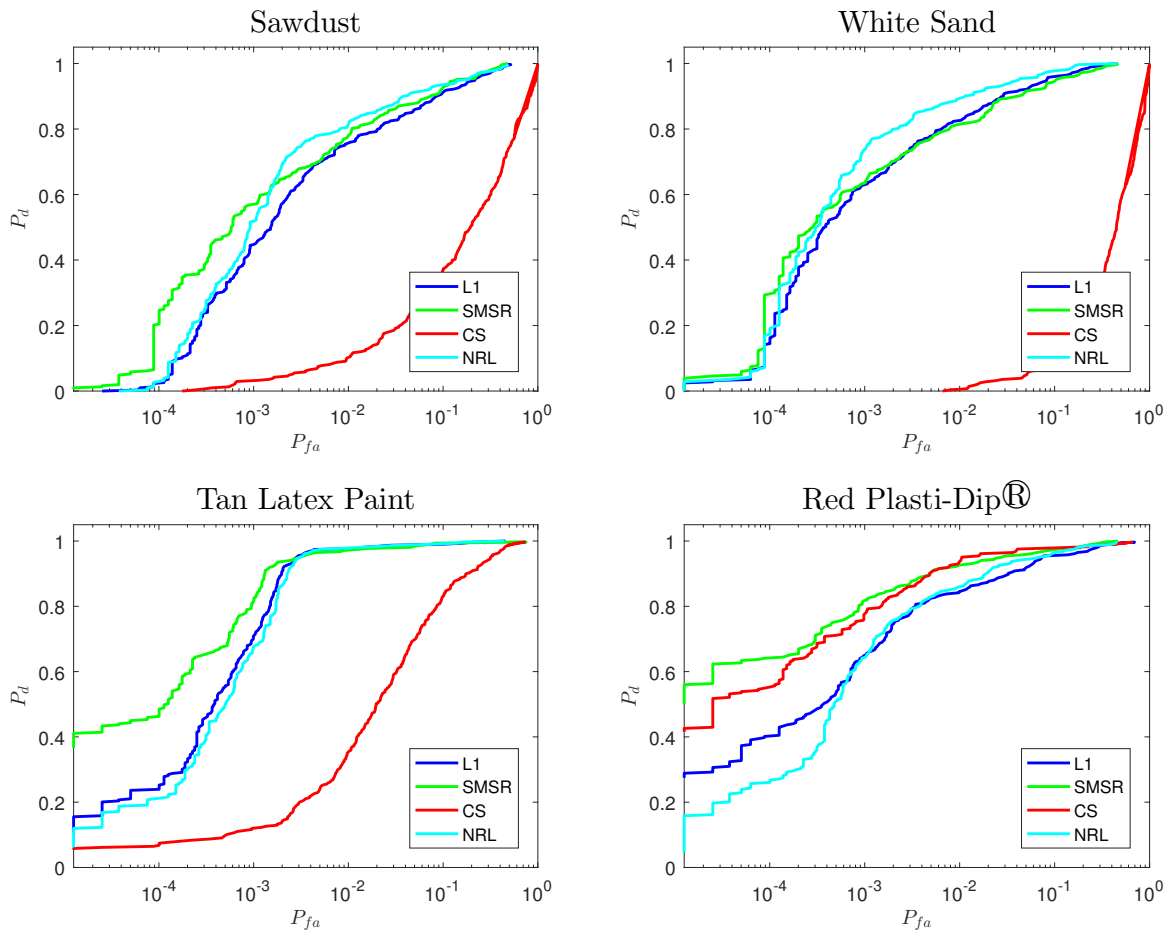


Figure 5.1: ROC Curves for each indicated target material class resulting from the L1, SMSR, CS, and NRL corrected image cubes.

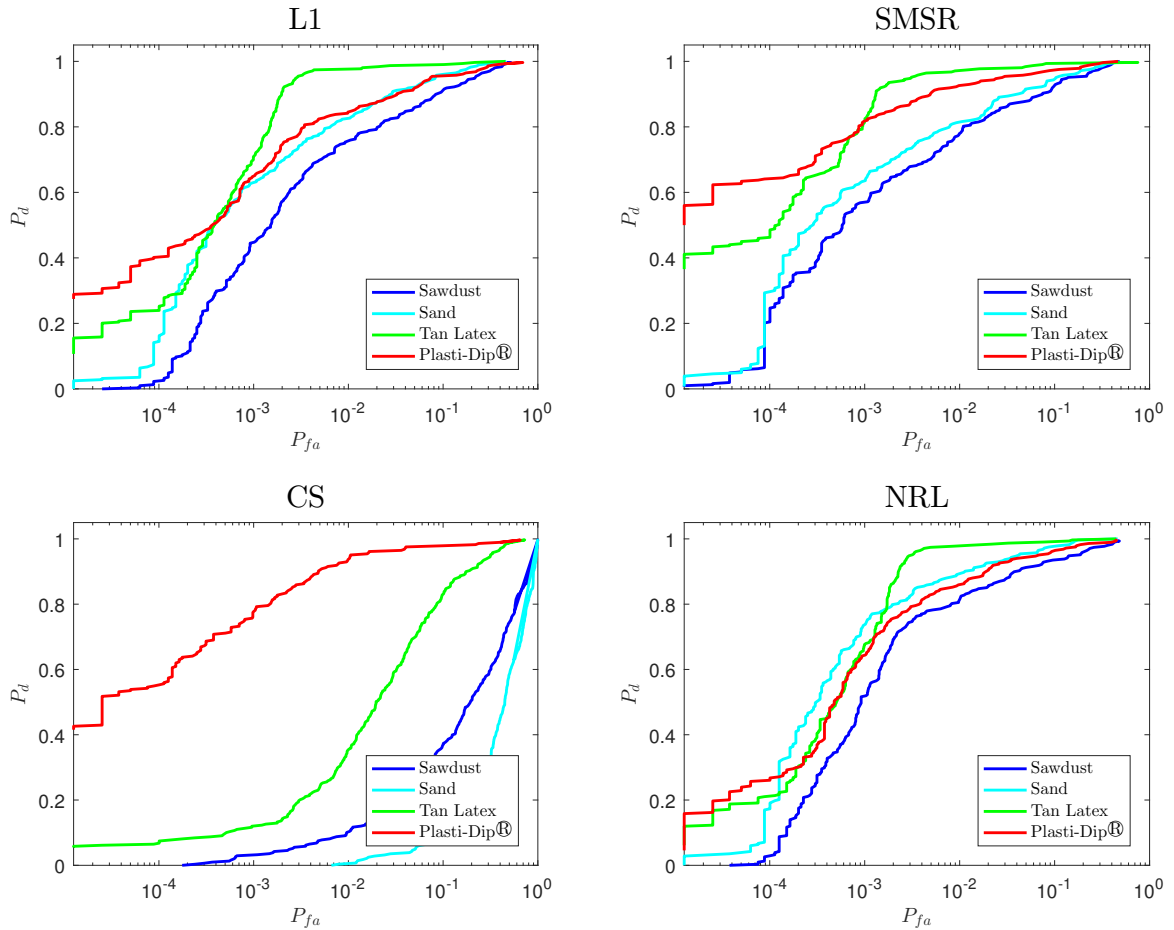


Figure 5.2: ROC curves from Fig. 5.1 organized according to correction type.

To better understand target-background separability in conjunction with the ROC results, histograms were computed from each ACE detection map for the target and background classes. The sixteen histogram plots, corresponding to each ROC curve in Fig. 5.2, are displayed in Fig. 5.3. The histograms illustrate how the high separable materials' ACE score distributions sit at a further distance away from the background, correlating with improved ROC curve performance. When comparing the L1 and SMSR results, the improvement in separability, while not dramatic, is clearly observed. The NRL results show

Table 5.1: PCC score between each target material spectrum and the mean scene-extracted grass signature from the L1, SMSR, CS, and NRL image cube.

Target Class	PCC Score			
	L1	SMSR	NRL	CS
Sawdust	0.9652	0.952	0.96638	0.46518
Sand	0.4331	0.41102	0.45383	0.10468
Tan Latex	0.7016	0.67482	0.71221	0.27346
Red Plasti-Dip [®]	0.4436	0.41665	0.44925	0.19508

improved separability for sand and sawdust, while reduced separability in the latex and rubberized paint histograms. The poor performance of the CS algorithms is also observed, where target histograms for sawdust and sand have become fully inseparable from the background distribution.

Finally, SCR values were computed corresponding to each ROC curve result and are displayed in Table 5.2. SCR scores provide a numerical assessment of the ROC curve where a higher score reflects a steeper rise in the knee of a curve. SCR values were computed using the median ACE score from each target class and the standard deviation of the ACE scores for the grass background pixels. The SCR values largely follow the trends observed in the ROC curves for each algorithm; however, it is important to note that these median results do not reflect the performance at lower false alarm rates.

Table 5.2: Target Class SCR for each corrected image cube.

Material	L1	SMSR	NRL	CS
Sawdust	3.2571	3.5148	3.9604	0.8731
Sand	3.7948	3.5519	4.4840	0.1446
Tan Latex	7.7100	7.9153	8.0725	2.5178
Red Plasti-Dip [®]	4.8811	5.5756	4.9555	4.7885

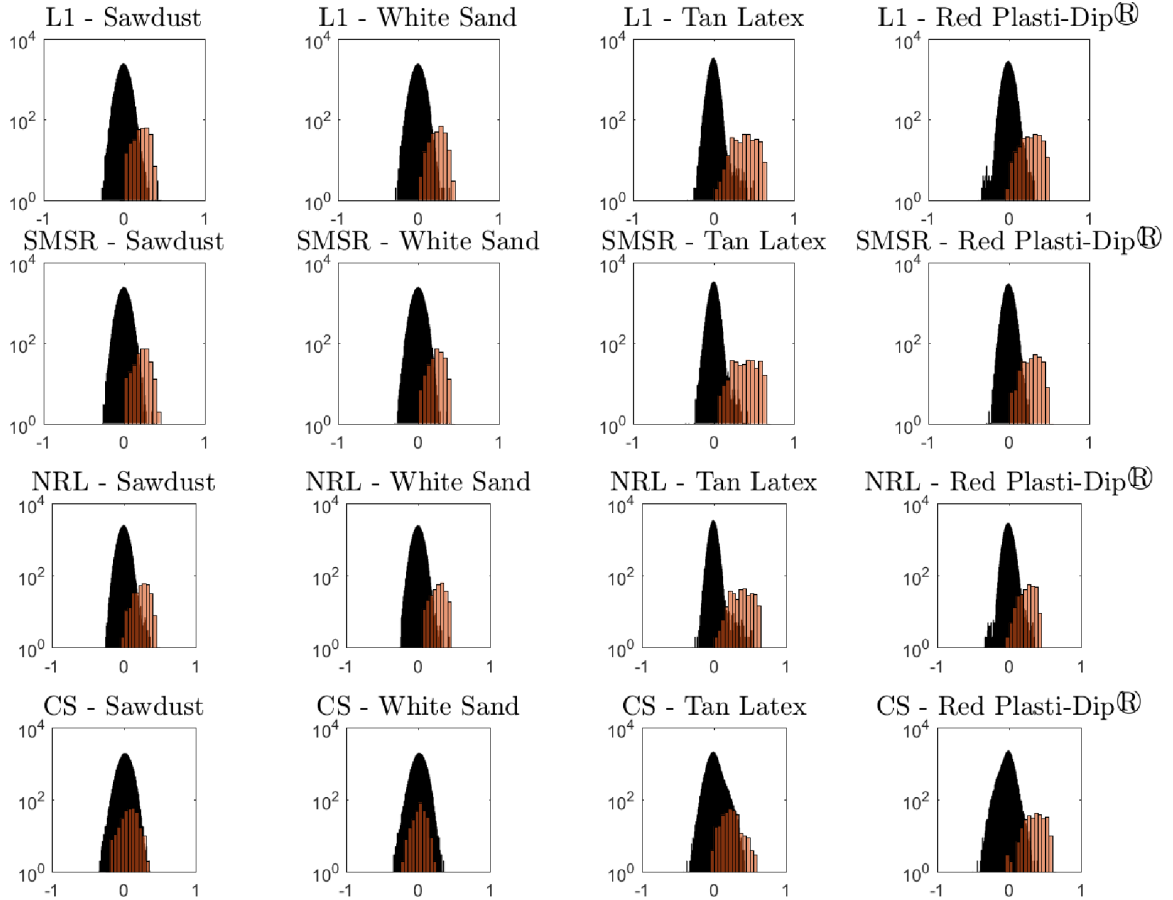


Figure 5.3: Histograms of the grass background (dark blue) and indicated target materials (light orange) corresponding to each ROC curve in Fig. 5.2.

5.2 Target Detection Performance as a Function of RFPN

To better understand the effect of RFPN on target detection performance, an image cube was corrupted with controlled levels of random noise and corresponding ROC curves were computed for each target material class. Since it is common in practice to obtain a recent offset map for calibration, we focused on introducing RFPN as random perturbations about the gain. We created such RFPN in the gain map using a normal

distribution with a mean of 1 and standard deviation σ_N . In the simulation, values of $\sigma_N = \{0.025, 0.05, 0.075, 0.1, 0.125, 0.15\}$ were used, which corresponds to SNR values of $\{0.998, 0.997, 0.993, 0.986, 0.980, 0.971\}$, respectively. We chose the SMSR-corrected image cube shown in Figure 4.1 as the baseline “clean” image cube to corrupt in this study. A single band image from each cube after applying RFPN at each noise level is shown in Figure 5.4 along with its corresponding RX map. For this study, a Monte Carlo simulation was performed using 50 trials at each noise level. Within each trial, a random noise gain map was generated and applied to the clean image cube. The SMSR algorithm was then applied to the corrupted cube and an ELM atmospheric correction was applied. The ACE detection map was then computed in each case and averaged across each trial’s results. ROC curves were then generated from these averaged ACE maps.

The ROC curves corresponding to these noise-degraded image cubes for each target material class are shown in Fig. 5.5 with corresponding target-background histograms shown in Figures. 5.6 and 5.7. The SCR values of each target material class for each noise level were computed and are displayed in Table 5.3. Figure 5.5 demonstrates that increasing levels of gain RFPN have an overall adverse effect on target detection performance. The trend can also be observed in the histogram plots of Figures 5.10 and 5.11, which is particularly apparent for the tan latex target material. For the Plasti-Dip[®] material, the addition of random Gaussian noise is actually increasing detection performance. To better understand this result, we examined the standard deviations of the ACE target and background histograms, as well as the distance between their means, which we examine in more detail below.

The results from correcting each corrupted image cube with the SMSR algorithm are shown in Figure 5.8. Figure 5.9 presents the average ROC curves corresponding to each

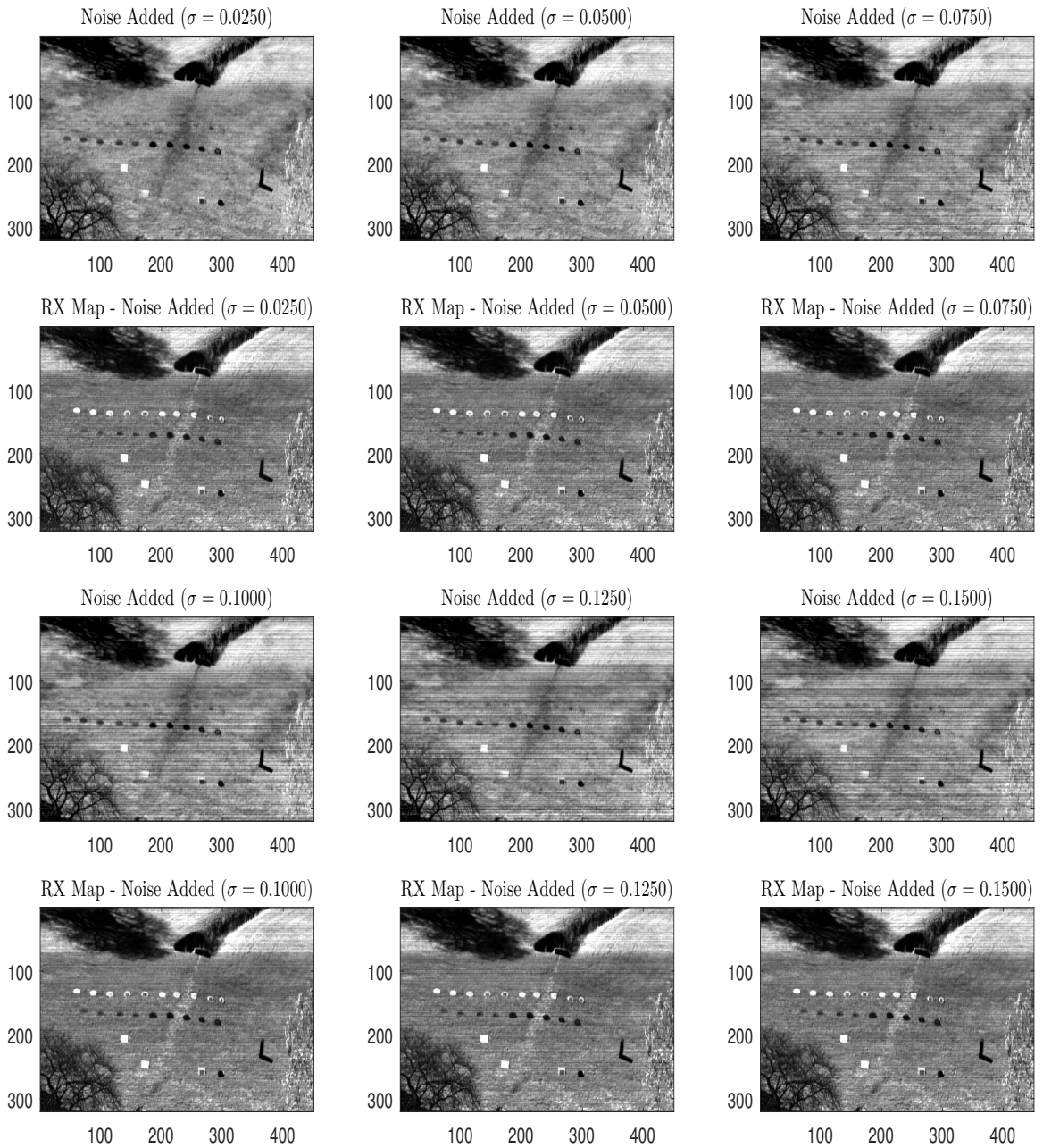


Figure 5.4: The first and third rows show the band 25 image from the clean SMSR cube with varying standard deviation levels. The second and fourth rows show the resulting RX map for the corresponding clean cube that is displayed above.

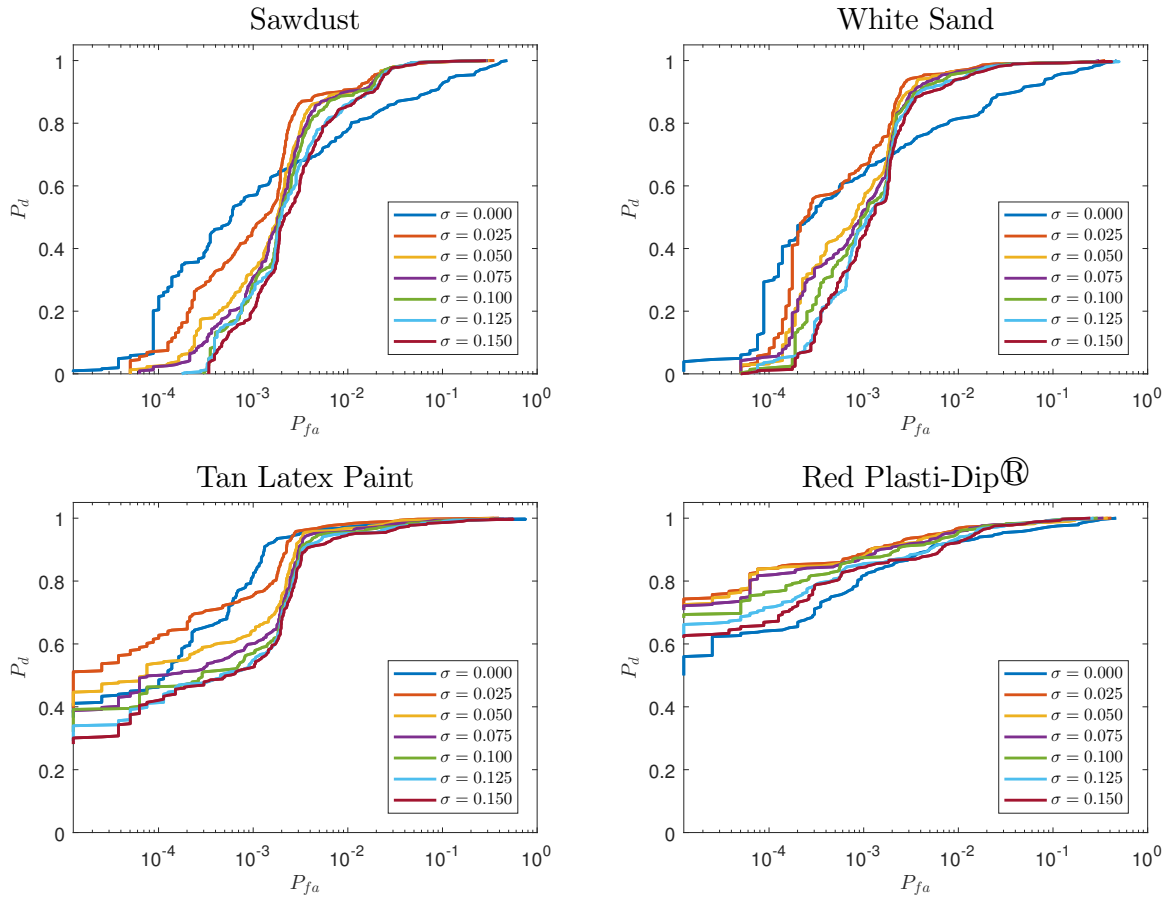


Figure 5.5: ROC Curves for each indicated target material class after introduction of gain RFPN at the indicated standard deviation level.

introduced noise level before and after application of the SMSR algorithm. Figures 5.10 and 5.11 display the histograms corresponding to the ROC curves in Figure 5.9. The ROC curves show a decrease in detection performance as the standard deviation increases, which matches with the SBNUC-corrected histograms.

Table 5.4 displays the standard deviation of the ACE histograms from each target and background class at each noise level, while Table 5.5 displays the corresponding differences

Table 5.3: SCR of Target Classes With/Without Introduced Noise

		Sawdust	Sand	Tan Latex	Red Plasti-Dip®
Noise Added	$\sigma = 0.025$	7.0405	8.4988	12.447	10.677
	$\sigma = 0.050$	6.9455	8.5597	11.144	10.907
	$\sigma = 0.075$	7.0594	8.5286	10.56	11.278
	$\sigma = 0.10$	6.8132	8.4454	9.9154	11.508
	$\sigma = 0.125$	6.5633	8.1727	9.6142	10.895
	$\sigma = 0.150$	6.2888	7.9959	9.3454	10.877
Noise Corrected	$\sigma = 0.025$	5.0745	5.588	7.1547	2.1216
	$\sigma = 0.050$	3.7119	4.4763	5.3018	1.4067
	$\sigma = 0.075$	3.2713	4.0107	4.2173	1.2213
	$\sigma = 0.10$	2.8891	3.5852	3.6587	1.1631
	$\sigma = 0.125$	2.854	3.3979	3.4388	1.1062
	$\sigma = 0.150$	2.6182	3.249	3.3353	0.99362

between each target class and background. As the standard deviation of the noise is increased, the distance between the target and background means decreases. This indicates an average decrease in separability, while we observe an increase in background standard deviation. Theoretically, the standard deviation of the ACE target distributions should also increase, yet we observe an opposite trend in Table 5.4. This phenomena is illustrated conceptually in Figure 5.12. The mean of the ACE background distribution shifts to the right when noise is introduced in addition to an increase in standard deviation. Conversely, the ACE target distributions shift leftward; however, we observe a decrease in the target histogram's standard deviation. As a result, the median SCR scores are skewed higher than the 0-noise added case. At lower probability of the false alarm rates, there is not a gradual increase in the ROC curve. Instead, the curve depicts a tighter, steeper knee at the median due to the mean-shifted histogram and tails off afterwards. This can be directly observed in the ROC curves of 5.9.

Table 5.4: Standard Deviation of Target Distributions

		Sawdust	Sand	Tan Latex	Red Plasti-Dip®
Noise Added	$\sigma = 0.025$	0.075998	0.068734	0.14595	0.16374
	$\sigma = 0.050$	0.075202	0.070022	0.13791	0.16644
	$\sigma = 0.075$	0.074726	0.072291	0.13397	0.16271
	$\sigma = 0.10$	0.072587	0.072232	0.12977	0.15606
	$\sigma = 0.125$	0.072649	0.069099	0.12766	0.15119
	$\sigma = 0.150$	0.069597	0.069213	0.1244	0.14438
Noise Corrected	$\sigma = 0.025$	0.035736	0.041231	0.096524	0.01877
	$\sigma = 0.050$	0.026024	0.035594	0.078659	0.01598
	$\sigma = 0.075$	0.023868	0.033561	0.068499	0.013668
	$\sigma = 0.10$	0.022506	0.033866	0.065089	0.013012
	$\sigma = 0.125$	0.020903	0.031458	0.058976	0.0121
	$\sigma = 0.150$	0.020574	0.033099	0.059126	0.012961

Table 5.5: Distance between the Means of Target and Background Histogram Distributions

		Sawdust	Sand	Tan Latex	Red Plasti-Dip®
Noise Added	$\sigma = 0.025$	0.24603	0.28041	0.40347	0.43362
	$\sigma = 0.050$	0.24912	0.29017	0.3624	0.43713
	$\sigma = 0.075$	0.24971	0.29166	0.34682	0.42638
	$\sigma = 0.10$	0.24546	0.2886	0.33273	0.41038
	$\sigma = 0.125$	0.23993	0.28026	0.32186	0.38995
	$\sigma = 0.150$	0.23227	0.27433	0.31232	0.37473
Noise Corrected	$\sigma = 0.025$	0.18315	0.21116	0.26362	0.079767
	$\sigma = 0.050$	0.13563	0.16345	0.20399	0.057224
	$\sigma = 0.075$	0.12724	0.15106	0.17602	0.052512
	$\sigma = 0.10$	0.11847	0.14396	0.16355	0.054551
	$\sigma = 0.125$	0.11583	0.13828	0.15569	0.049745
	$\sigma = 0.150$	0.11052	0.13547	0.15208	0.04632

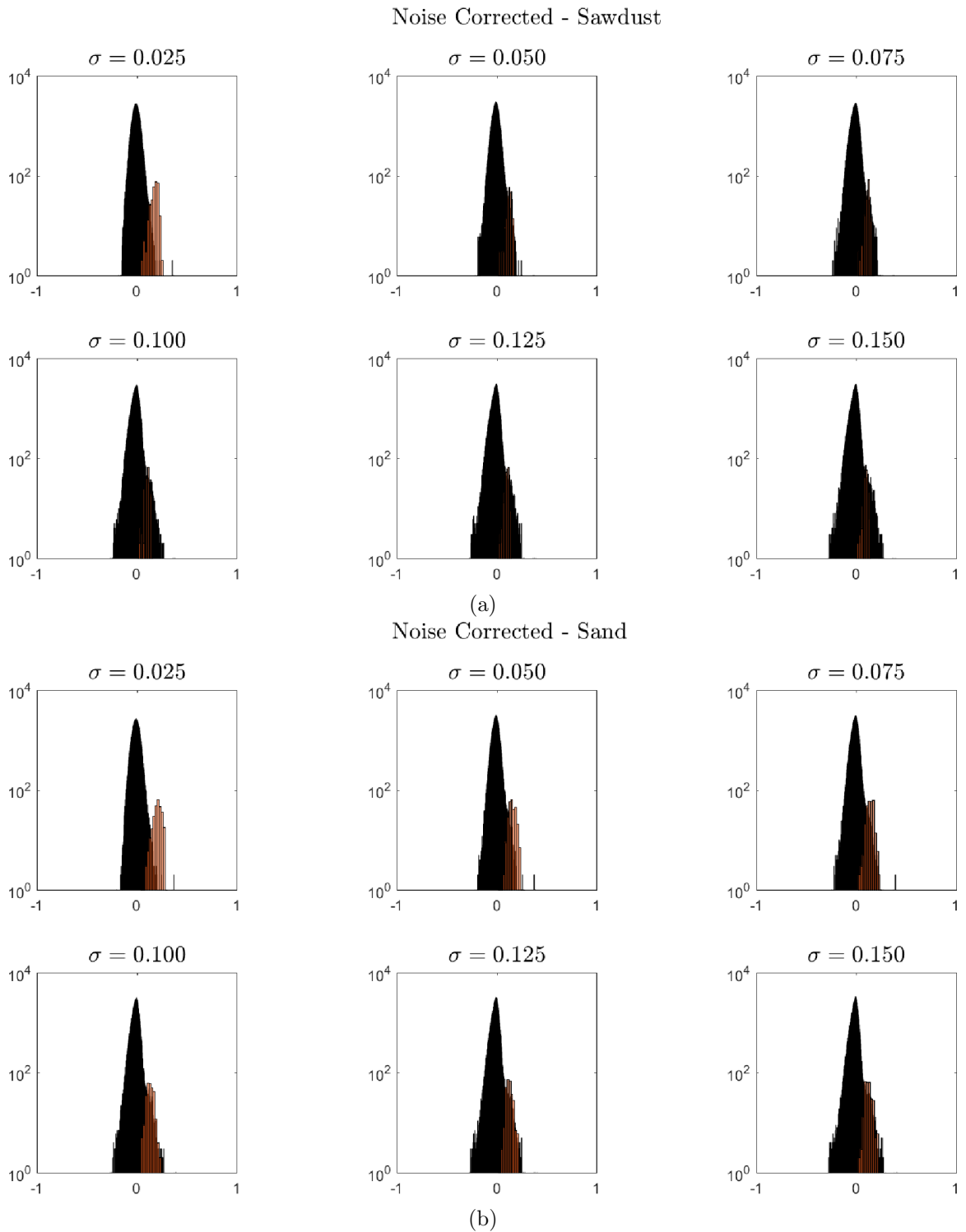


Figure 5.6: Histograms of ACE scores between for background and target (Sawdust and Sand) classes of the noise added image cubes.

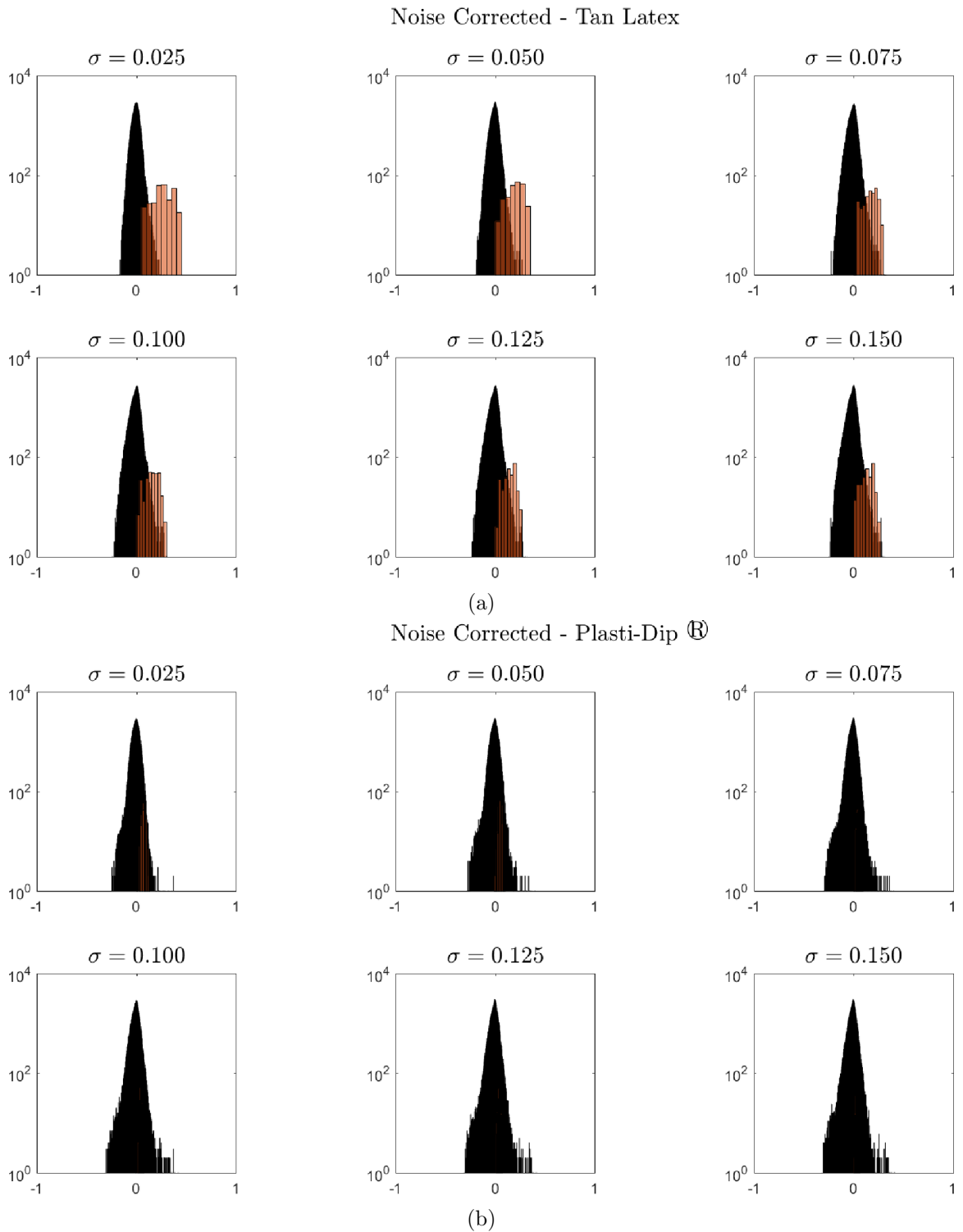


Figure 5.7: Histograms of ACE scores between for background and target (Tan Latex and Red Plasti-Dip[®]) classes of the noise added image cubes.

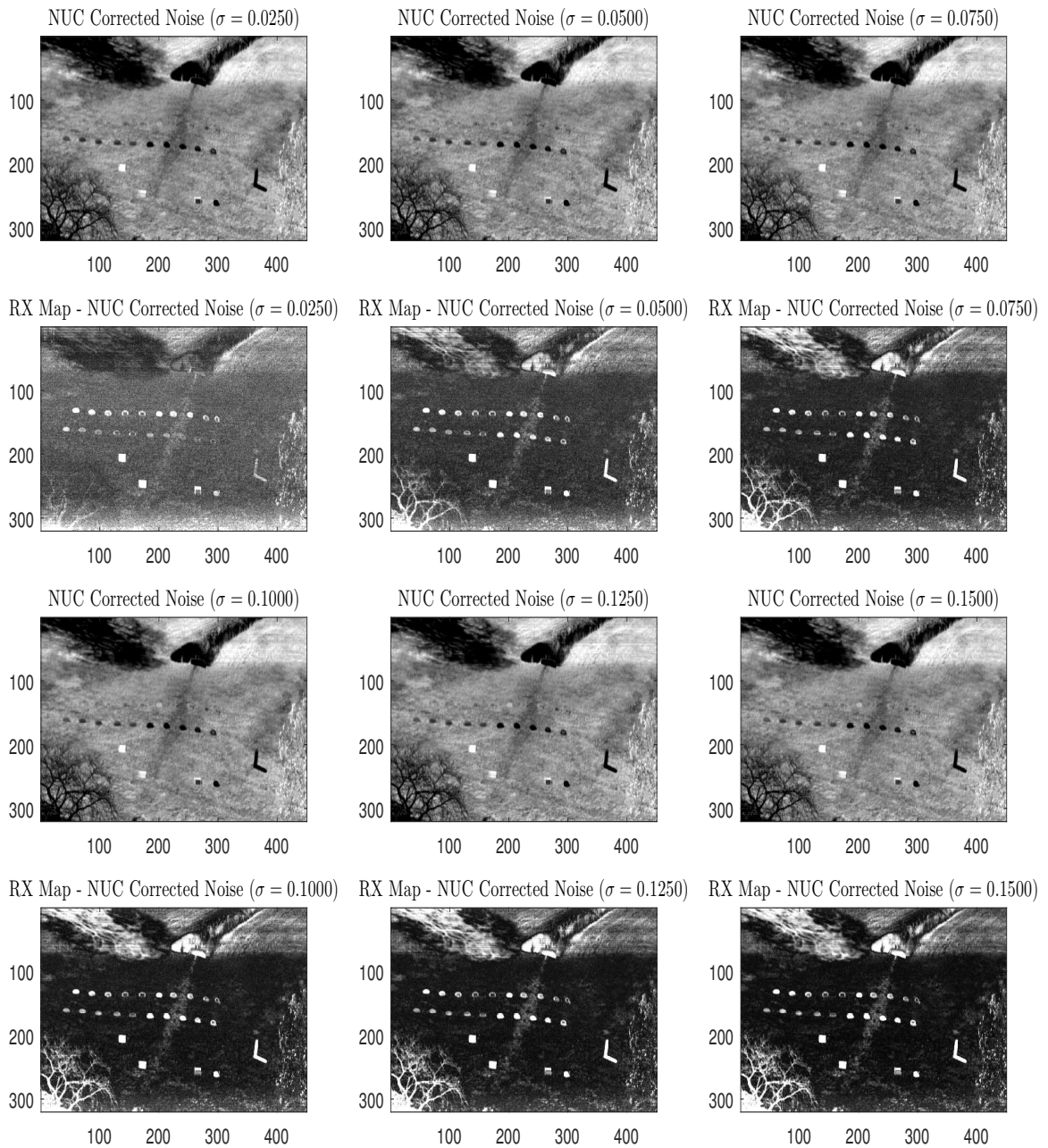


Figure 5.8: The first and third rows show the band 25 image from the NUC applied cube that had varying standard deviation levels applied. The second and fourth rows show the resulting RX map for the corresponding clean cube that is displayed above.

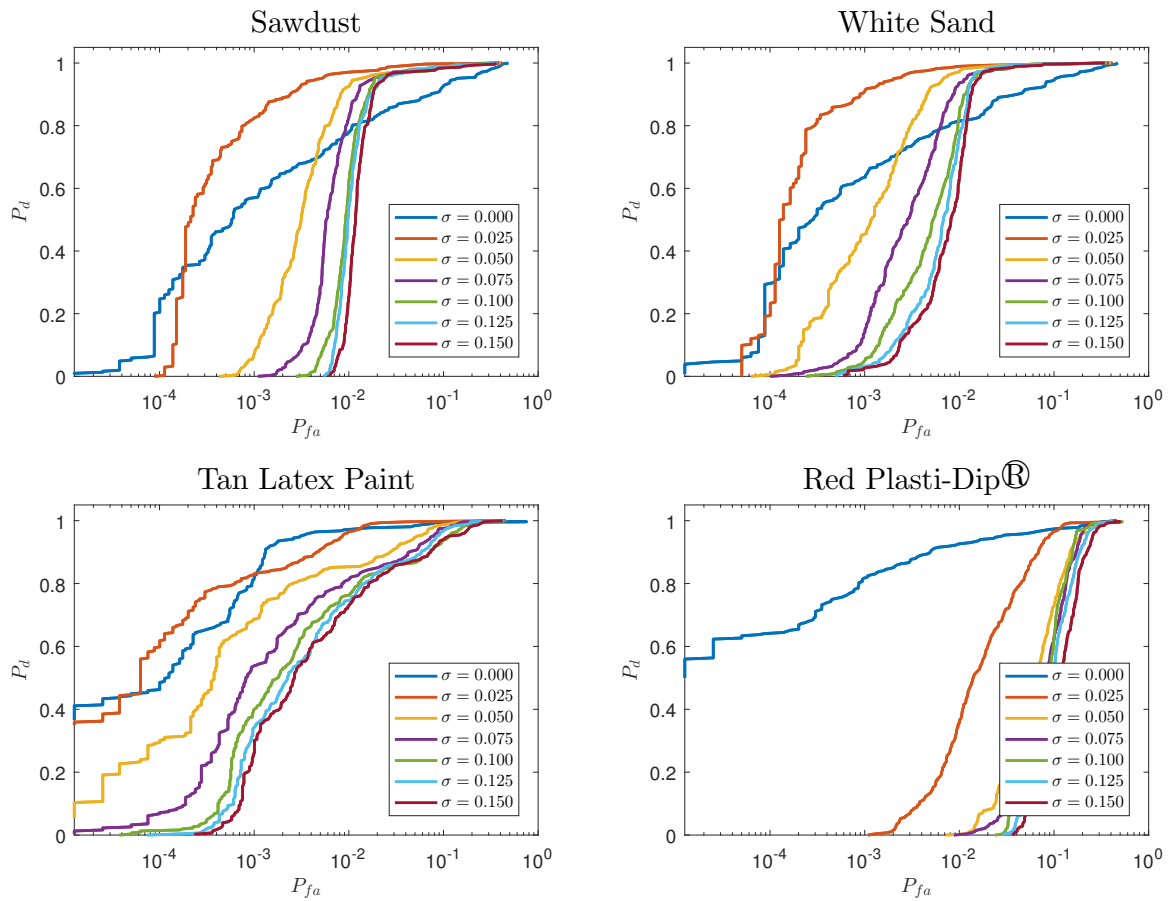


Figure 5.9: ROC Curves for each indicated target material class after introduction of gain RFPN and correction via SMSR SBNUC algorithm at the indicated standard deviation level.

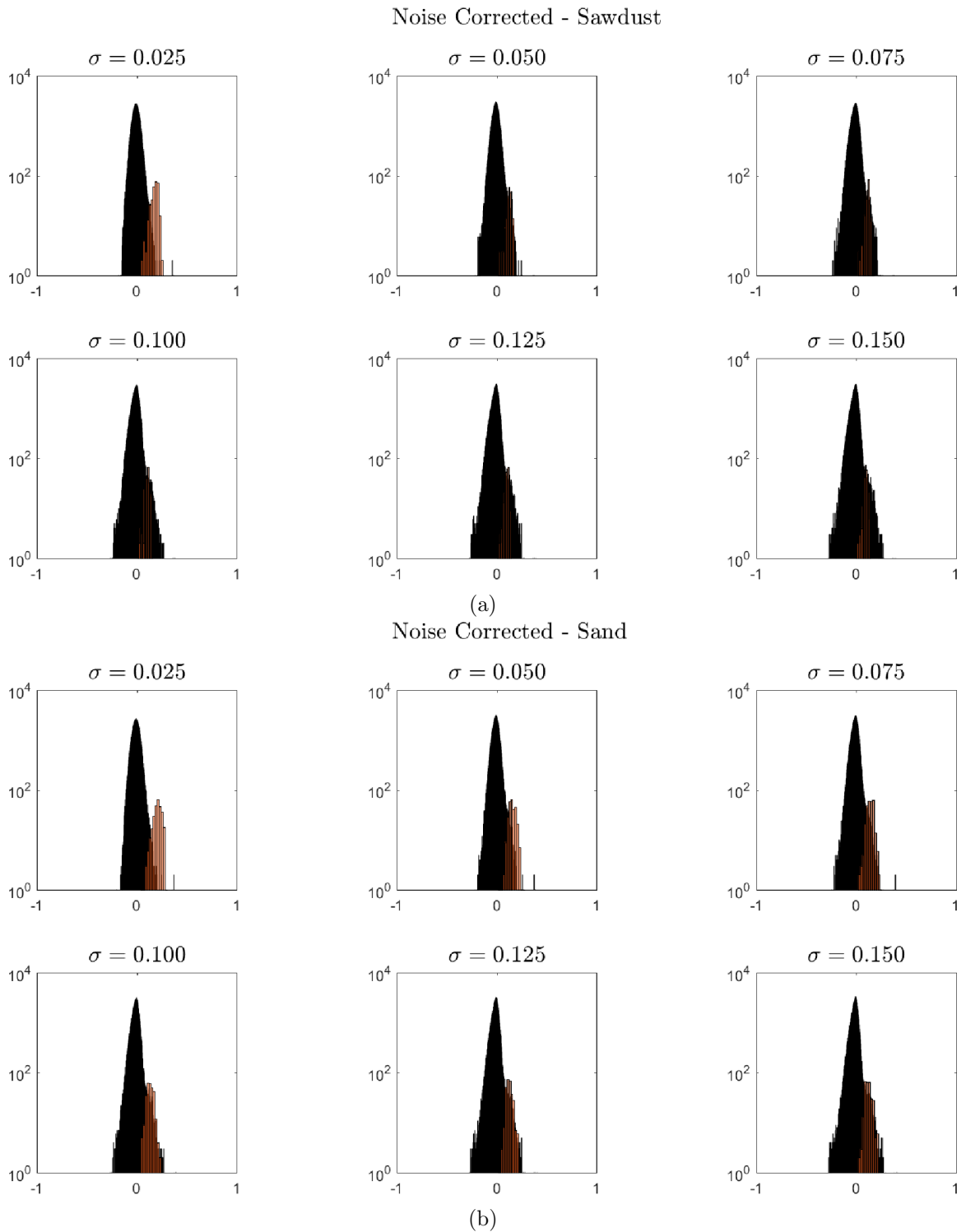


Figure 5.10: Histograms of ACE scores between for background and target (Sawdust and Sand) classes of the noise corrected image cubes.

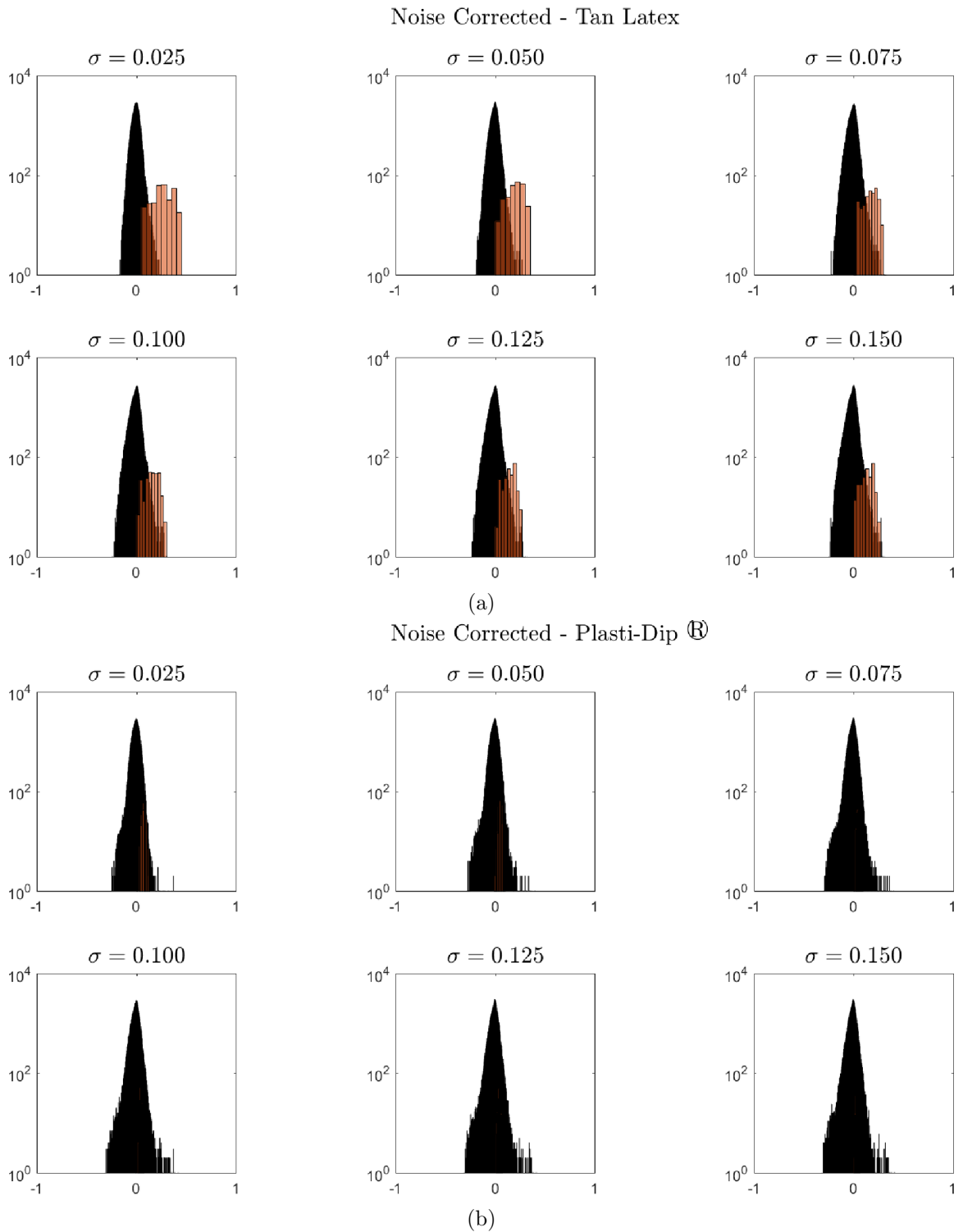
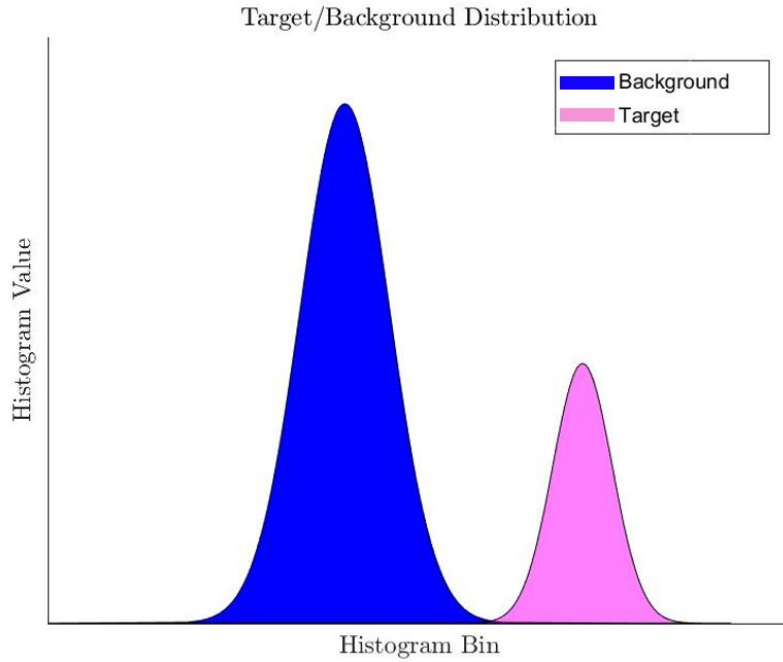
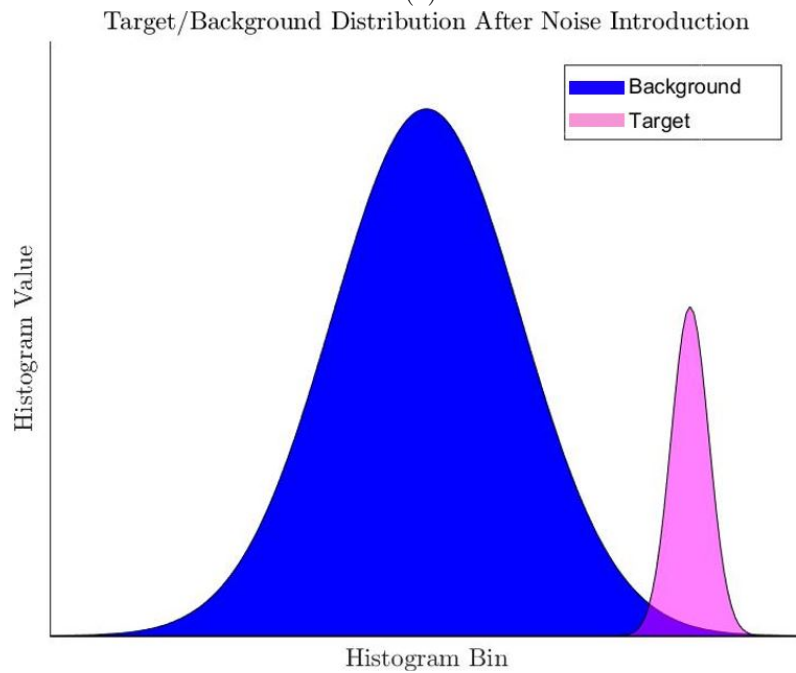


Figure 5.11: Histograms of ACE scores between for background and target (Tan Latex and Red Plasti-Dip[®]) classes of the noise corrected image cubes.



(a)



(b)

Figure 5.12: Target/Background ACE histograms before and after introduced noise correction.

CHAPTER VI

CONCLUSION

In this work we investigate the effect that residual fixed pattern noise has upon target detection performance in hyperspectral image data. A data collection experiment was carefully designed and conducted to support this study. As part of the experiment target panels were designed which contained materials that have different inherent levels of separability from natural background. Furthermore, we designed the target panels such that controlled levels of mixing between the target material and background were achieved. Such targets allowed for studying the effect of residual fixed pattern noise as a function of material separability in addition to allowing for high fidelity receiver operating characteristic detection curves to be obtained. The sun illumination angle during the data collection was not optimal during that time of year; however, the collected data showed considerable utility for this study. We were able to show that residual fixed pattern noise affects the detectability of each target class differently based upon its inherent separability from the background. A moderate inherently separable material from the background is affected the most by the inclusion of SBNUC algorithms. Furthermore we demonstrated through adding simulated noise to the data how target detection performance degrades as a function of material separability. Finally, we investigated the ability of a particular SBNUC algorithm to remove the added RFPN.

In future work we hope to repeat this experiment under more favorable illumination and atmospheric conditions, namely, a time where the sun is at the most optimal angle pointing directly at the targets for each scenario. Moreover, we want to create a data set that can be used across the hyperspectral community as a benchmark for analyzing the performance

of newly designed SBNUC algorithms. Overall, many lessons were learned from this study that will direct how we proceed in future data collections of this type.

BIBLIOGRAPHY

- [1] G. Holst, *CCD Arrays, Cameras, and Displays*, SPIE Opt. Eng. Press, Bellingham, Wash. (1996).
- [2] A. Milton, F. Barone, and M. Kruer, “Influence of nonuniformity on infrared focal plane array performance,” *Opt. Eng.* **24**, 855–862 (1985).
- [3] D. Perry and E. Dereniak, “Linear theory of nonuniformity correction in infrared staring sensors,” *Opt. Eng.* **32**, 18531859 (1993).
- [4] A. Friedenber and I. Goldbatt, “Nonuniformity two-point linear correction errors in infrared focal plane arrays,” *Opt. Eng.* **37**, 1251–1253 (1998).
- [5] S. Torres and M. Hayat, “Kalman filtering for adaptive nonuniformity correction in infrared focal plane arrays,” *J. Opt. Soc. Am. A* **20**, 470480 (2003).
- [6] D. Scribner et al., “Adaptive nonuniformity correction for IR focal plane arrays using neural networks,” *Proc. SPIE* **1541**, 100109 (1991).
- [7] R. Hardie et al., “Scene-based nonuniformity correction with reduced ghosting using a gated LMS algorithm,” *Opt. Express* **17**, 1491814933 (2009).
- [8] J. Harris and Y. Chiang, “Nonuniformity correction using constant average statistics constraint: Analog and digital implementations,” *Proc. SPIE* **3061**, 895–905 (1997).
- [9] B. Ratliff, M. Hayat, and J. S. Tyo, Radiometrically accurate scenebased nonuniformity correction for array sensors, *J. Opt. Soc. Am. A* **20**, 18901899 (2003).
- [10] B. Ratliff, M. Hayat, and J. S. Tyo, An algebraic algorithm for nonuniformity correction in focal-plane arrays, *J. Opt. Soc. Am. A* **19**, 17371747 (2002).
- [11] B. Ratliff, M. Hayat, and J. S. Tyo, Generalized algebraic scene-based nonuniformity correction algorithm, *J. Opt. Soc. Am. A* **22**, 239249 (2005).
- [12] W. Black and J. Tyo, “Feedback-integrated scene cancellation scene-based nonuniformity correction algorithm,” *J. Electron. Imaging* **23(2)**, 023005 (2014).
- [13] C. Zuo et al., Scene-based nonuniformity correction algorithms based on interframe registration, *J. Opt. Soc. Am. A* **28(6)**, 11641176 (2011).
- [14] R. Hardie et al., “Scene-based nonuniformity correction using video sequences and registration,” *Appl. Opt.* **39**, 12411250 (2000).
- [15] W. ONeil, Dither image scanner with compensation for individual detector response and gain, United States Patent 5, 514 , 865 (1996).

- [16] B. M. Ratliff and J. R. Kaufman, "Scene-based correction of fixed pattern noise in hyperspectral image data using temporal reordering," *Optical Engineering* **54(9)**, 093102 (2015).
- [17] R. Leathers, T. Downes, and R. Priest, "Scene-based nonuniformity corrections for optical and SWIR pushbroom sensors," *Opt. Express* **13**, 5136-5150 (2005).
- [18] S. Adler-Golden, S. Richtsmeier, P. Conforti and L. Bernstein, "Spectral Image Destriping using a Low-dimensional Model," *Proc. SPIE* **8743**, 87431Q, (2013).
- [19] Q. Yuan, L. Zhang, and H. Shen, Hyperspectral image denoising employing a spectralspatial adaptive total variation model, *IEEE Trans. Geosci. Remote Sens.* **50(10)**, 36603677 (2012).
- [20] M. Bouali and S. Ladjal, Toward optimal destriping of MODIS data using a unidirectional variational model, *IEEE Trans. Geosci. Remote Sens.* **49(8)**, 29242935 (2011).
- [21] P. Meza et al., Applied nonuniformity correction for striping noise removal in hyperspectral images, in *Proc. of Latin American Remote Sensing Week*, pp. 716731 (2010).
- [22] N. Acito, M. Diani, and G. Corsini, Subspace-based striping noise reduction in hyperspectral images, *IEEE Trans. Geosci. Remote Sens.* **49(4)**, 13251342 (2011).
- [23] J. Kerekes, "Receiver operating characteristic curve confidence intervals and regions," *IEEE Geoscience and Remote Sensing Letters* **5(2)**, 251–255 (2008).
- [24] M. K. Griffin and H. H. K. Burke, "Compensation of hyperspectral data for atmospheric effects," *Lincoln Laboratory Journal* **14(1)**, 29-54 (2003).
- [25] I. Reed and X. Yu, "Adaptive multiple-band CFAR detection of an optical pattern with unknown spectral distribution," *IEEE Trans. Acoustics, Speech, and Sig. Proc.* **38(10)**, 1760–1770 (1990).
- [26] S. Kraut and L. Scharf, "The CFAR adaptive subspace detector is a scale-invariant GLRT," *IEEE Trans. Sig. Proc.* **47(9)**, 2538–2541 (1999).